International Journal of Heat and Mass Transfer 218 (2024) 124774

Contents lists available at ScienceDirect

International Journal of Heat and Mass Transfer

journal homepage: www.elsevier.com/locate/ijhmt

Experimental investigation of additively manufactured high-temperature heat exchangers

Marco Fuchs *, Julian Bodemer, Stephan Kabelac

Institute of Thermodynamics, Leibniz University Hannover, An der Universität 1, 30823 Garbsen, Germany

ARTICLE INFO

Keywords:
Additive manufacturing
Heat exchanger
High temperature
Heat transfer coefficients
Friction-factors
Experimental

ABSTRACT

This article examines various additively manufactured heat exchangers for high-temperature applications. The heat exchangers differ in terms of their internal fin structure as well as optimizations in terms of manufacturing quality. Starting from a reference fin type, optimizations with focus on low pressure drop and high heat transfer are performed. The heat exchangers are investigated experimentally, focusing on the laminar flow regime between $60<Re<600$. By means of a presented evaluation algorithm, the Nusselt numbers for the different fin types and designs are determined. The investigations show that even the smallest manufacturing deviations result in up to 70–120% higher f-factors and up to 30% higher Nu numbers. Taking these manufacturing deviations into account in the design process leads to very good agreement with the numerically determined values and the influence of surface roughness is comparatively small. Furthermore, the influence of internal heat radiation is of minor importance for the heat exchangers considered here.

1. Introduction

The manufacturing of compact heat exchangers by means of additive manufacturing (SLM/LPBF) is becoming increasingly important, as it allows heat exchangers to be easily adapted to specific requirements and new geometric boundary conditions. Examples of additively manufacturable structures include lattice structures, minimal surface structures and also specific optimizations in terms of heat transfer and pressure drop.

Lattice Structures are designed to provide increased turbulence and thus higher heat transfer by means of a large number of struts, as shown in Shen et al. [1], Ekade et al. [2] and Liang et al. [3]. Other examples are so-called minimal surface structures, e.g. gyroids, which are investigated in Dixit et al. [4], Tang et al. [5] and Dassi et al. [6]. Thus, additive manufacturing can be used to enable specific optimizations to structures to influence flow in terms of heat transfer and pressure drop, as presented in Alexandersen et al. [7], Dede et al. [8], and Pilagatti et al. [9], among others that are presented in the reviews done by Dbouk et al. [10].

However, the development of such structures is accompanied by the issues of manufacturability, fabrication accuracy, and the influence of surface roughness.

Bichnevicius et al. [11] compared additively and conventionally fabricated louvered fins experimentally and found significant deviations of 203% in pressure drop and 105% in the overall heat transfer coefficient compared to the conventionally fabricated version. Similarly, even a 72% higher pressure drop was found when manufactured by a different SLM/LPBF machine. The authors attribute this to the increased surface roughness and, as a result, an earlier changeover to turbulent flow. However, no information is provided on hydraulic diameters and the relative surface roughness. Vafadar et al. [12] investigated additively and conventionally manufactured fin elements and also find increased pressure losses of the additively manufactured variants, with no clear trend in the heat transfer. It is argued that the increased surface roughness results in better heat transfer, but the increased porosity of the material leads to lower thermal conductivity and thus again to lower overall performance. Niknam et al. [13] provide a review of various additively manufactured heat exchangers and also conclude that pressure drop, in particular, due to the increased surface roughness is a sensitive variable in the design of the corresponding apparatus. Saltzman and Lynch [14] investigated the influence of additively manufactured heat exchangers with off-set strip fin structures made of an aluminium alloy or, alternatively, by a polymer. The authors found that the agreement between the calculation and the heat exchanger made of polymer is significantly better than for the variant made of aluminium. In the laminar region, deviations between the numerical calculations and experiments of about 20% are found, in the turbulent region up to

* Corresponding author.
E-mail addresses: fuchs@ift.uni-hannover.de (M. Fuchs), julian.bodemer@stud.uni-hannover.de (J. Bodemer), kabelac@ift.uni-hannover.de (S. Kabelac).

https://doi.org/10.1016/j.ijheatmasstransfer.2023.124774
Received 26 May 2023; Received in revised form 15 September 2023; Accepted 28 September 2023
Available online 6 October 2023

Nomenclature

A	Area (m^2)
A^*	Thermally conductive cross-section (m^2)
b_{ch}	Channel width (m)
B	Heat exchanger width (m)
$\overline{c}_p$	Mean specific isobaric heat capacity (J/(kg·K)
C	Coefficient for Nu or f-factor correlation (-)
d_h	Hydraulic diameter (M)
g	Acceleration of gravity (m/s^2)
h	Height (mm)
H	Heat exchanger height (m)
k	Overall heat transfer coefficient ($W/(m^2 \cdot K)$)
K_p	Dimensionless axial resistance coefficient (-)
$K_{\mathrm{geo,f,i,j}}^{\gamma_{f,ij}}$	Geometric parameter coefficient for Nu, f-factor correlation (-)
l	Length of a single fin passage (m)
L	Heat exchanger length (m)
$\dot{m}$	Mass flow rate (kg/s)
$n_l,\ n_q$	Number of fin passages along the flow direction (-)
N	Number of channels (-)
n	Coefficient for Nu- or f-factor correlation (-)
N	Maximum number of measuring points (-)
p	Pressure (Pa)
P	Perimeter (m)
$\dot{Q}$	Heat flow (W)
Rz	Roughness (µm)
s	Error function (-)
T	Temperature (K)
u	Velocity (m/s)
$\dot{W}$	Heat capacity rate (W/K)

Greek formula symbols

α	Heat transfer coefficient ($W/(m^2 \cdot K)$)
$\gamma_{Nu/f,i,j}$	Coefficient for geometric parameter in Nu/f-factor correlations (-)
δ_t	Thermal boundary layer thickness (m)
Δh	Height difference (m)
Δp	Pressure loss (Pa)
ΔT_{log}	Logarithmic temperature difference (K)
ζ	Pressure loss coefficient (-)
η_0	Surface efficiency (-)
η_{fin}	Fin efficiency (-)
λ	Heat conductivity (W/(m·K))
ρ	Density (kg/m^3)

Dimensionless number

Nu	Nusselt number ($\mathrm{Nu} = \frac{\alpha \cdot d_h}{\lambda_f}$)
Pr	Prandtl number ($\mathrm{Pr} = \frac{\eta \cdot c_p}{\lambda}$)
Re	Reynolds number ($\mathrm{Re} = \frac{u \cdot d_h}{\nu}$)
j	Colburn-j-factor ($j = \frac{\mathrm{Nu}}{Re \cdot \mathrm{Pr}^{\left(\frac{1}{3}\right)}}$)
f	Fanning-friction-factor f ($f = \frac{\Delta p \cdot d_h}{2 \cdot \rho \cdot u^2 \cdot L}$)

Sub- and superscripts List of Abbreviation

axe	axial direction
c	cold fluid
cal	calculated
con	contraction
Dist	distributor
ex	expansion
exp	experimental
f	fluid
fin	fin
f, fr, fric	f-factor, friction
h	hot fluid
ht	Heat transfer
i,	counting variable, c or h
in	inlet
j	counting variable
m	mean
max	maximum
min	minimum
out	outlet
s, solid	solid
tot	total
w	water
approx.	approximately
CAD	computer aided design
FO	flow-optimized
HTO	heat-transfer-optimized
Num	Numerical
Vers.	Version

50% higher f-factors. Furthermore, they detect a changeover to turbulent flow at lower Reynolds numbers, which is determined using a Laser Doppler Velocimetry method. Statements on the deviation of the hydraulic diameter due to the surface roughness are not given. Also Saltzman and Lynch [15] studied 5 heat exchangers with off-set structures, with two additive manufactured heat exchangers made of polymer and three made of metal. They again determined good agreement with the correlations for the polymer heat exchangers. For the heat exchangers made of metal, a maximum of 20% higher f-factors in the laminar region and 40% higher f-factors in the turbulent region were determined. Huang et al. [16] studied the roughness of additively manufactured tubes and varied the relative roughness in the range 0.008 - 0.417. They found that the agreements in the laminar region for low roughness up to 0.071 is in good agreement with the values for a smooth tube. From a relative roughness of 0.095 and more, the deviations increase to +15 - 20%. For further increasing roughness, a considerable increase of the f-factor is determined, as well as a shift of the critical Reynolds number towards smaller values. However, it should be noted in these investigations that a constant hydraulic diameter is assumed for all cases investigated. The smaller flow cross-section that arises, especially at high relative roughness, is not taken into account. The change in hydraulic diameter just by variation of roughness is typically underestimated in literature. Ning et al. [17] studied three additively manufactured heat exchangers (316L stainless steel) with different internal structures and compared them with the numerically determined data. The data show some scatter in the heat transfer coefficient between -10% and +19% compared to the numerical values. The pressure drop reaches a maximum of 14 - 25% higher than the numerically calculated values, depending on the structure used. No information is given about the measured roughness and possible manufacturing deviations, but they are mentioned as a possible influence on the results.

In this paper, six additively manufactured compact heat exchangers with different internal fin types will be investigated with respect to heat transfer and pressure drop. In this context, the influence of manufacturing defects, such as bulges, and roughness on heat transfer and pressure drop is discussed and the results are compared to numerical calculations. Furthermore, an evaluation methodology is presented by means of which the unknown heat transfer coefficients can be

determined.

2. Method

2.1. Investigated Heat Exchangers

The heat exchangers investigated are plate-fin heat exchangers equipped with different internal fin types. The material used for the heat exchangers tested here is stainless steel 316L.

Fig. 1 shows an example of such a heat exchanger and the different fin types. The heat exchangers are composed of several layers, with the layers alternately serving as a flow channel for the hot and cold fluid. Each layer consists of two manifolds and one main section, with only the main section, 66mm in length, being equipped with the appropriate heat transfer fin type. A counterflow configuration is present in the main area, while the manifold areas have a crossflow characteristic. In total, all the heat exchangers presented have seven layers, three for the hot side and four for the cold side. The heat exchangers have identical external dimensions, and the construction volume of each heat exchanger is ~0.45 litre, of which about ~0.15 litre is accounted for the manifolds. The exact dimensions are not published for reasons of confidentiality. The design of the internal fin types was initially based on off-set strip fin heat exchangers and then optimized with respect to heat transfer and low irreversible entropy production. The heat transfer areas, minimum flow cross-section and hydraulic diameter are summarized in Table 1. The applications for which these heat exchangers are developed are within the high temperature range up to 900°C and for low pressure losses of <50mbar only. Especially the last aspect leads inevitably to the situation that the heat exchangers have to be operated in the laminar range with comparatively small Reynolds number. This further has the consequence that turbulent effects decay quickly and do not persist over a longer flow path [18]. Therefore, the fin types are developed and optimized under the premise of generating as little pressure loss as possible outside the thermal boundary layer, which leads to a reduction of recirculation areas and detachment regions.

The development of the fin type "Reference" is based on geometrical parameter variations presented in Fuchs et al. [19]. Based on the parameters presented there, an entropically optimal parameter combination giving the lowest entropy production rate in an average operating range is determined, which gives the fin type called "Reference". Based on the resulting streamlines, two different structural adjustments are made, see also Fig. 2. For the "FO" version, the fins are shaped in such a way that a reduction of the front stagnation area is achieved. This is intended to prevent flow detachment in the front region of the fin and thus make better use of the area of the thin thermal boundary layer and thus of high heat transfer mechanisms. Furthermore, the available solid cross-sectional area within the fin for better heat conduction is increased in this region, which leads to a higher fin efficiency. The fins, which are getting continuously thinner in the downstream direction, are intended to reduce frictional pressure loss through thick hydrodynamic boundary layers precisely in those areas where heat transfer is reduced anyway due to thicker thermal boundary layers. For the “Heat Transfer Optimized” (HTO)" fin type, the fin design is based on the forming of the thermal boundary layer. The fins are shaped in such a way that the thermal boundary layer is reduced with increasing fin length, in order to keep heat transfer at a high level. At the same time, however, the hydrodynamic boundary layer is also thinned out, resulting in high velocity gradients and thus high shear stresses, which lead to increasing frictional pressure losses. However, by combining these increased frictional pressure losses with the presence of a thin thermal boundary layer, the resulting pressure losses contribute directly to heat transfer. Furthermore, a negative longitudinal displacement reduces the detachment area in the wake of the fin rows, thus avoiding unnecessary pressure losses.

Table 1
Geometric parameters for the different fin types.

	Heat transfer area [m²]	Minimum cross section area [mm²]	Hydraulic diameter [mm]
“Ref”	0.136	1000	1.55
„HTO“	0.163	723	1.18
„FO“	0.151	869.4	1.42

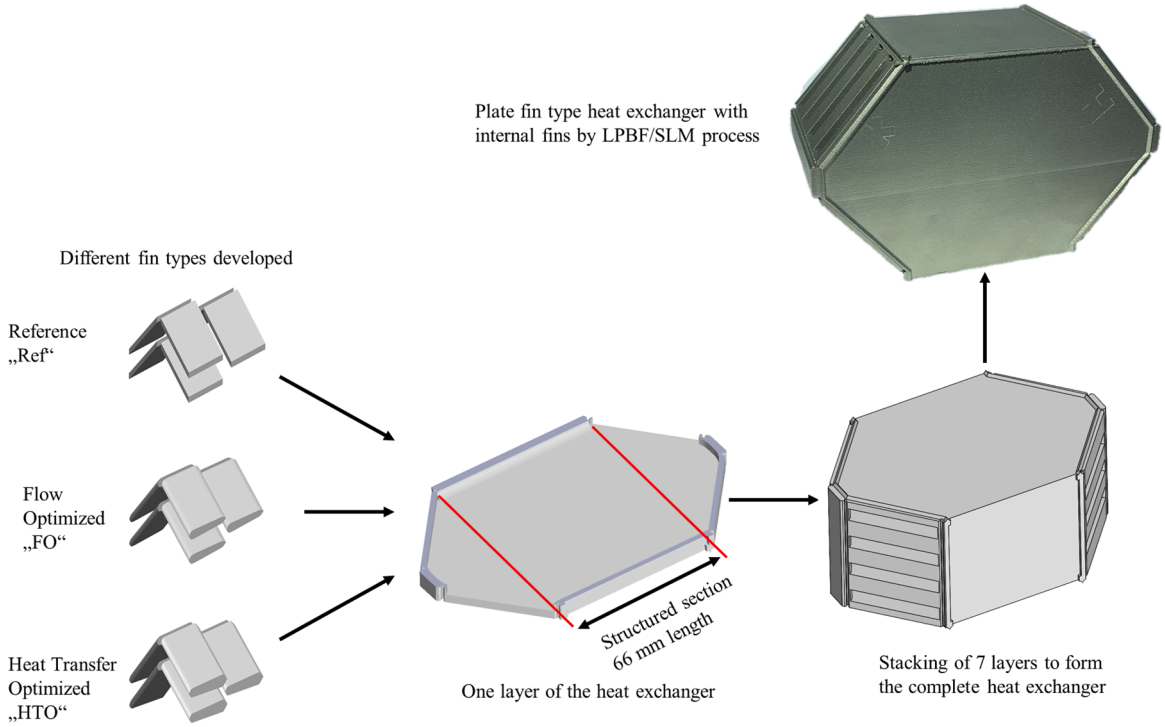

Fig. 1. Design principle of the heat exchangers to be tested with different heat transfer fin types ("Ref", "FO", "HTO") located in the “structured section”.

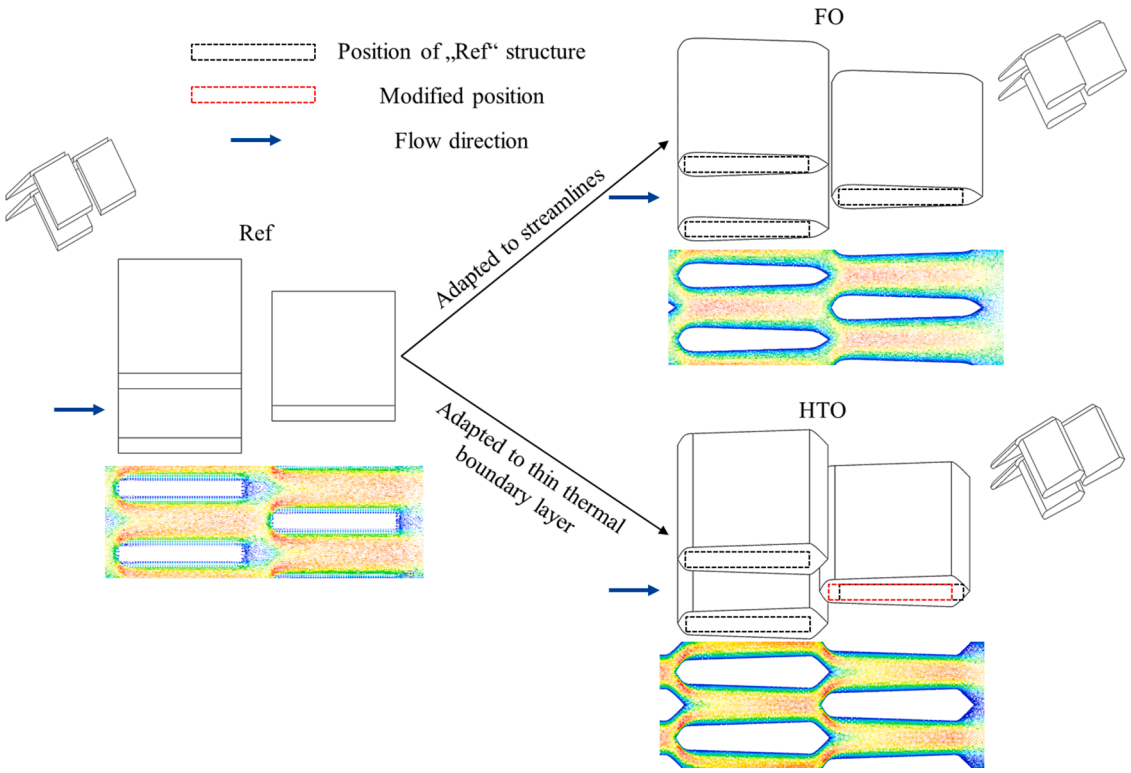

Fig. 2. Details of the different optimized fin geometries: The shape of the “FO”-fins is adapted to the streamlines forming around the “Ref”-fin type to reduce wake and detachment areas. The shape of the “HTO”-fins is adapted to form a thin thermal boundary for increasing heat transfer coefficients and to reduce wake areas by modify the position of the following fin row.

2.2. *Detailed analysis of the heat transferring fin types*

There are already many studies on additively manufactured heat exchangers in the literature, as presented in Section 1. As explained, the manufacturing accuracy and the roughness are often cited as a major factor of uncertainty for the predictability of heat transfer and pressure loss. Therefore, in this section, a comparison between the manufactured component with the corresponding CAD model will be carried out on the basis of the “HTO”-fin type, the main deviations will be discussed.

Fig. 3 shows the X-ray micrographs of the "Heat Transfer Optimized" fin type. For this investigation only a small section of the heat exchanger is manufactured, containing one half of the hot side and one half of the cold side channel. The manufacturing direction of the printing process (SLM/LPBF technique) is vertical, as indicated. The most obvious deviation is the increased roughness of the surface compared to the CAD model. Furthermore, corresponding manufacturing inaccuracies can be seen at the tip of the fins, such as bulges, which do not appear in the CAD model. It can also be stated that the shaping of the fin types and the details such as the changed fin tracking can be reproduced comparatively well by additive manufacturing. In order to check how well the 3D printing can reproduce the contour of the fin, a BestFit comparison is also carried out using the "GOM Inspector" [20] program from the Zeiss company. The corresponding deviations are shown in Fig. 4. The analysis shows quite clearly that the deviations on the upper side of the fins are comparatively small, averaging only +8-16% of the fin thickness of the CAD model. Furthermore, the deviations are evenly distributed over the entire surface, there is no preferred direction, neither towards the base of the fins nor towards the fin tip. The analysis of the fin down side

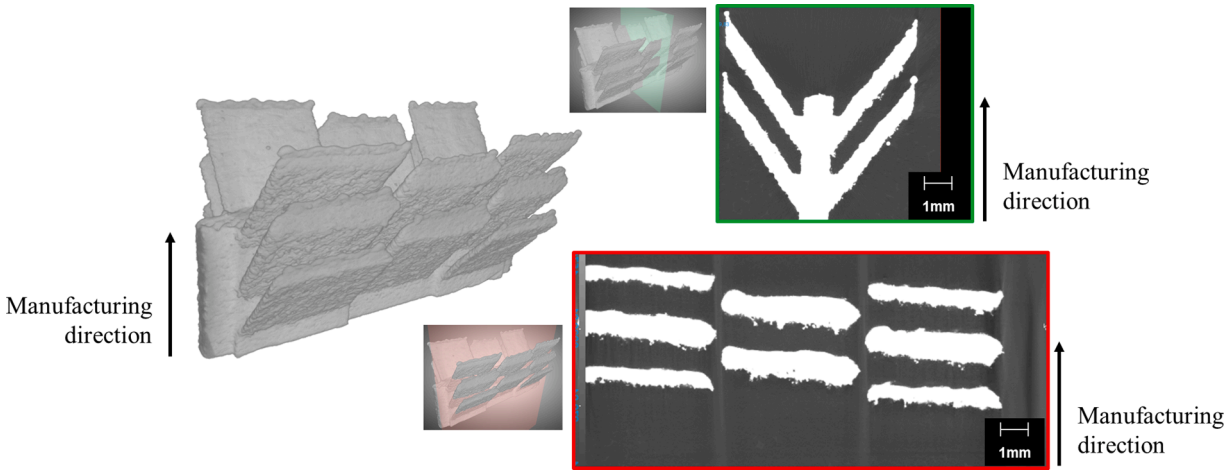

Fig. 3. Left: X-Ray microscopy of the “HTO”-fin type, right: details of the fins.

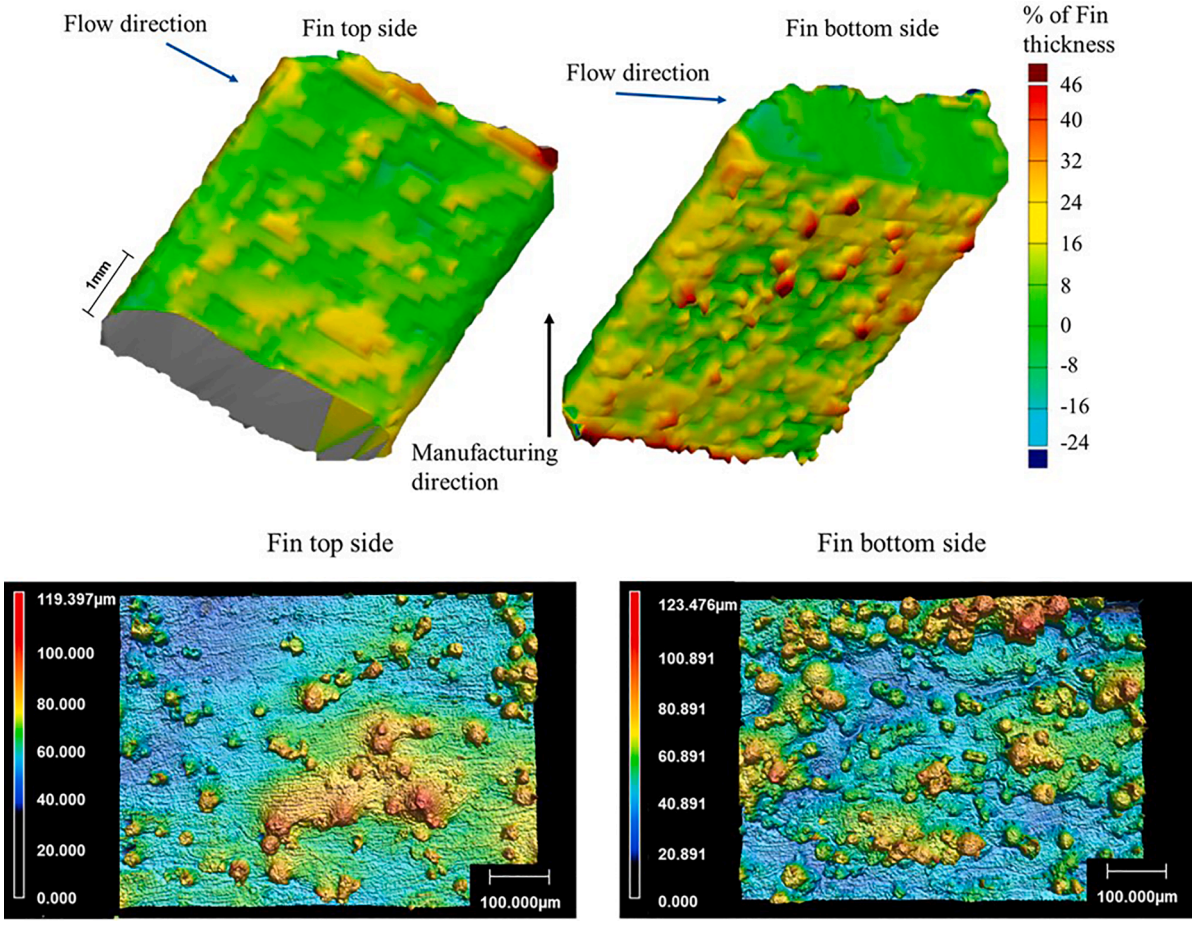

Fig. 4. Top: Deviations between the X-Ray microscopy and the original CAD-Model Bottom: Surface topography of the fin top side and bottom side.

shows that the deviations compared to the CAD model are on average about +23% of the fin thickness and are also subject to significantly larger deviations (from the lowest to the highest roughness -4 to +46%). The analysis of the deviations further shows that no significant difference in the deviations can be detected along the fin height (from fin root to fin tip). This means that no deformation of the fins and thus no change in geometry (e.g. lowering of the fin tip) occurs during the manufacturing process, which would have a corresponding effect on the subsequent measurement result. The frontal stagnation point as well as the outflow edge of the fin show no major deviations compared to the CAD model. In direct comparison, significant manufacturing inaccuracies can be seen at the tip of the fin, amounting to up to 46% of the fin thickness. These manufacturing inaccuracies significantly reduce the flow cross-section, thus they force the flow into the open areas between the fins. This leads to flow acceleration and thus to an increasing pressure drop. Furthermore, the size of these manufacturing inaccuracies at the fin tips is stochastically distributed, which makes the design less resilient and requires greater safety factors. The analysis shows clearly that additive manufacturing can in principle well reproduce the developed and optimized fin types, including details such as the fin pitch.

In addition to dimensional accuracy, the roughness of additively manufactured components is as already stated an important aspect, also shown in Fig. 4. For this purpose, the roughness values of both the lower and upper surfaces of the "HTO"-fin were measured. Fig. 4 shows the topography of the upper and lower sides of the fins. The analysis shows that the upper surface has an average roughness of $R_z = 25.2\ \mu$m and the lower surface an average roughness of $R_z = 63.1\ \mu$m, which is comparable with the values of Saltzmann et al. [21] and [22]. These data will serve in the further course of the article for the classification of the measurement results. Based on the analysis carried out, a slight modification for a second version of the same fin types is made. For this purpose, the design of the tip of the fins is shortened to create a flat terminating surface of max. 93 µm width for production, which prevents some of the manufacturing inaccuracies from forming. The two variants, referred to as version 1 and version 2, are shown in Fig. 5. A comparison of the flow cross sections in the CAD model shows that version 2 has less than 0.8% higher flow cross section than version 1.

2.3. Heat exchanger test bench

A test rig located at the Institute is used for the investigation of the different versions of heat exchangers. Fig. 6 shows a flow schematic and a photograph of a heat exchanger test section during installation. The connection is made by quick-fit flanges and clamps, and a mica-based high-temperature gasket resistant up to 1300°C is used as the flange gasket. Before each commissioning of a new test object, a leak test of all previously opened connections is carried out. The heat exchanger and the surrounding equipment is insulated by a high-temperature insulation wool ($\lambda_{ins} = 0.035$ W/mK). The test stand provides two air flows from the compressed air network, whose volume flows are each controlled by a MassFlowController (Bronkhorst F-203AV and Bürkert type 8746). The temperature of the air can be controlled by one heater each (with an electrical power of 8kW each), up to 900°C can be reached on the hot side and 750°C on the cold side. The temperatures at the inlet and outlet of the heat exchanger under test are measured with two type K thermocouples (diameter: 1 mm, 0.5 mm) each, which have been calibrated in advance by means of a block calibrator type Isotech Pegasus Advanced and a type R thermocouple as a reference thermometer. The thermocouples are placed in straight tubes about 140 mm long, at the inlet of each of which a mixing chamber is mounted in order

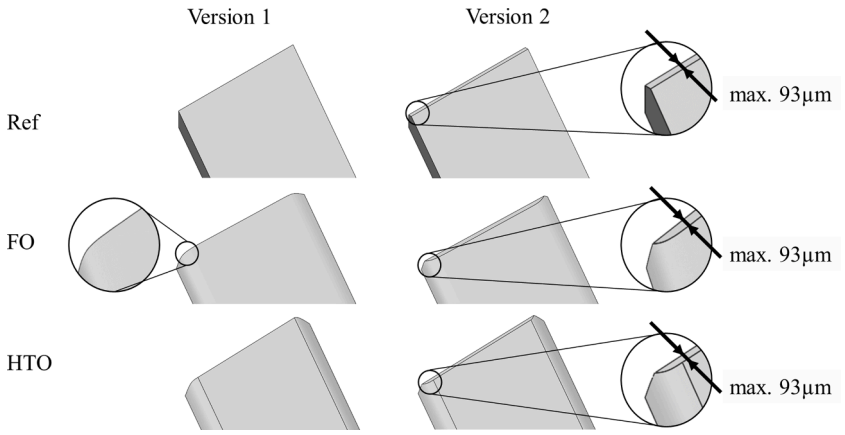

Fig. 5. Comparison of the fins in version 1 and modified in version 2. The modification takes place over the complete length of the fins to a maximum width of 93 µm.

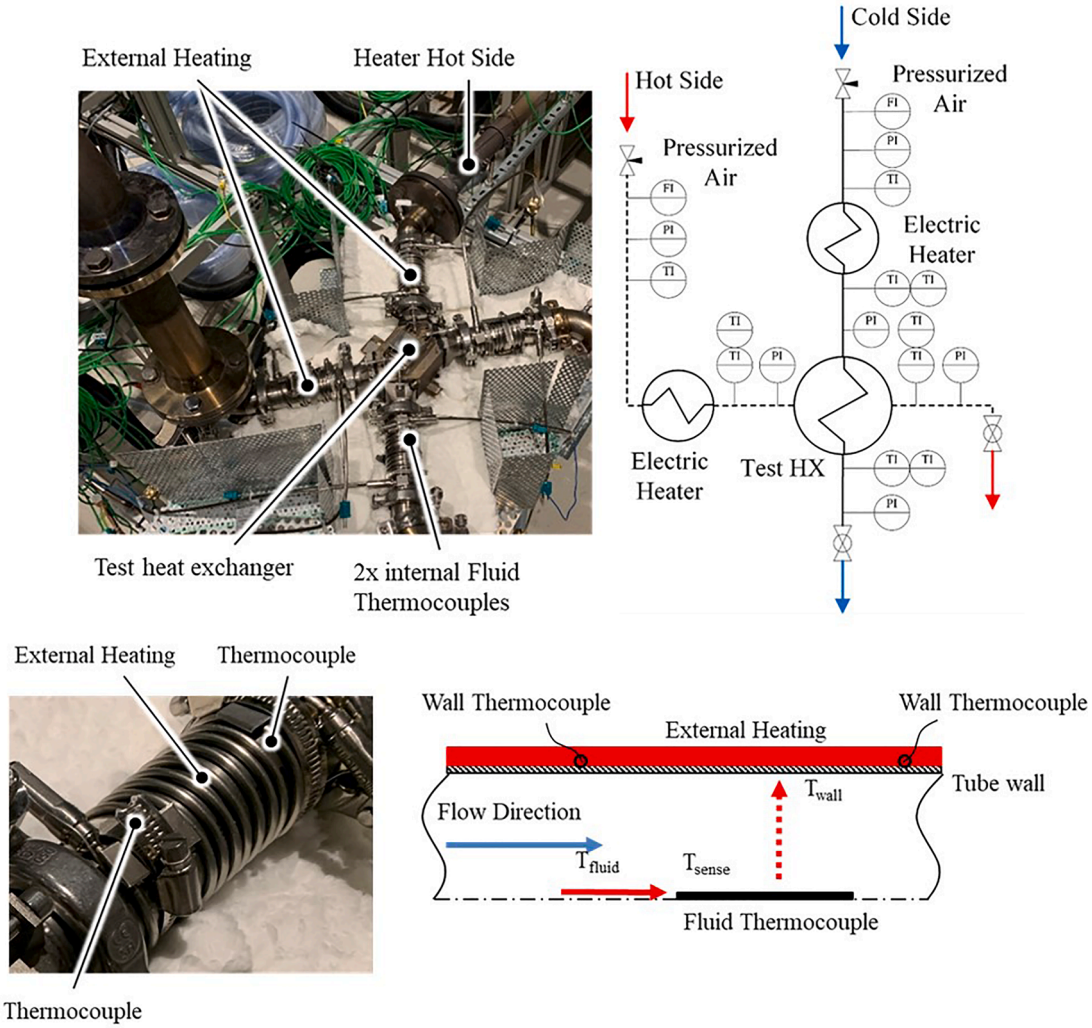

Fig. 6. Top: left: Picture of the test rig during heat exchanger installation before insulation, right: flow schematic of the test rig, Bottom: left: external heating to compensate radiation influence on the fluid thermocouples, right: principle of the external heating and corresponding heat flows (dotted line: Radiation between the thermocouple and the wall, solid line: convection between the fluid and the thermocouple).

to reduce a possible temperature profile across the cross-section and thus increase the measurement accuracy. Furthermore, these tubes are wrapped with heating tapes and equipped with two wall temperature measurements each, this serves to control the wall temperature in the area of the fluid temperature measurement. The aim of this additional heating of the tube wall is to adjust the wall temperature close to the fluid temperature to minimize the influence of thermal radiation on the fluid temperature measurement. The arrangement of the thermocouples and the heating as well as the principle is shown in Fig. 6. The control of the heating bands is as follows: the wall temperature is increased until a

constant difference of 1-2 K between wall and fluid temperature occurs, whereby the wall temperature is always below the fluid temperature. Mounting two wall thermocouples approximately 70 mm apart will also ensure an uniform temperature distribution along the length of the pipe, resulting in a lower radiation-based error in the fluid temperature measurement. This concept is superior to radiation shielded thermocouples. Flow distributors are welded to the heat exchangers manifolds to connect them to the four heated inlet and outlet tubes. Capillary tubes are inserted vertically onto the inlet and outlet section to enable the pressure loss measurement. The capillary tubes contain 4 holes across the length so that a pressure averaged over the cross-section is measured. The capillary tubes are placed directly at the inlet and outlet of the heat exchangers. Since, in addition to the heat exchangers presented here, various other ones with large pressure loss ranges are examined in this test rig. Therefore the pressure loss measurement must also be as accurate as possible over a large measuring range. Precision U-tube pressure gauges are ideal for this purpose, since their accuracy is constant over the entire measuring range and thus different heat exchangers can be examined with identical measuring technique. Furthermore, the U-tube manometers do not exhibit any drift, which also ensures long-term stability. The height difference at the U-tube manometer is converted to the pressure difference by $\Delta p_{tot} = \Delta h \cdot g \cdot \rho_w$, where ρ_w denotes the density of the distilled water in the manometer. The tests will be carried out at three different inlet temperature levels: 200/80°C, 400/80°C and 700/380°C. The working fluid is air, the Reynolds-Number of both flows is varied between 60 and 600. Furthermore the tests contain balanced as well as unbalanced flows up to $0.25 < \dot{W}_h/\dot{W}_c < 4$, where $\dot{W}_i = \dot{m}_i \cdot c_{p,i}$.

3. Evaluation methodology

By means of the experimental investigations, the Nusselt numbers, the pressure loss coefficients and other characteristic values are to be determined. These data will then be used for comparison with the numerically determined values in order to check the calculation accuracy as well as to evaluate the influence of manufacturing deviations.

3.1. Pressure loss coefficient (Fanning f-factor)

The pressure drop of the heat exchanger is composed of a total of five parts, the pressure drops at the inlet and outlet of the distributor ($\Delta p_{con,Dist}$ & $\Delta p_{ex,Dist}$), the friction pressure drop inside the finned section $\Delta p_{fric,fin}$ and the pressure drop due to contraction/expansion at the inlet and outlet of the finned area ($\Delta p_{con,fin}$& $\Delta p_{ex,fin}$). Thus the overall pressure drop is defined as follows (i indicates wether it is the hot or cold fluid)

$$\Delta p_{tot,i} = \Delta p_{con,Dist,i} + \Delta p_{con,fin,i} + \Delta p_{fric,fin,i} + \Delta p_{ex,fin,i} + \Delta p_{ex,Dist,i}. \quad (1)$$

The following simple equation [23] is used to calculate the pressure losses due to expansion and contraction.

$$\Delta p_{ex,con,i} = \zeta_{ex,con,i} \frac{\rho_{ex,con,i}}{2} u^2_{max,i}. \quad (2)$$

For the velocity u_{max}, the velocity in the smaller cross section is chosen throughout. The density is calculated with the temperatures at the inlet or outlet of the distributor or finned section. The determination of the loss coefficients $\zeta_{ex,con}$ is based on the diagrams according to Kays [24] for "multiple square tubes" for the Reynolds number Re_{max} and the respective flow area ratio.

With the knowledge of the expansion and contraction losses, the pressure losses can be reduced to the pressure loss due to friction. It thus follows

$$\Delta p_{fric,fin,i} = \Delta p_{tot,i} - \Delta p_{con,Dist,i} - \Delta p_{con,fin,i} - \Delta p_{ex,fin,i} - \Delta p_{ex,Dist,i}. \quad (3)$$

The pressure loss coefficient due to friction, the Fanning f-factor, is now calculated using the following equation.

$$f_i = \frac{\Delta p_{fric,fin,i} \cdot d_{h,i}}{2 \cdot \rho_{m,i} \cdot L \cdot u^2_{m,i}}. \quad (4)$$

For the hydraulic diameter, the value from Table 1 is used accordingly, and the velocity $u_{m,i} = \dot{m}_i / A_{min,i}\ \rho_{m,i}$ is determined at the narrowest cross section in each case, using an arithmetic mean value between inlet and outlet for the density $\rho_{m,i}$. The flowed-through channel length L is the same for all heat exchangers.

3.2. Experimental overall heat transfer coefficient

The Nusselt number and the surface efficiency can be determined by means of the experimentally determined overall heat transfer coefficient. This is calculated by means of the overall heat transfer equation via the inlet and outlet temperatures as well as the mass flow of the cold side

$$kA_{exp} = \frac{\dot{Q}_{cold}}{\Delta T_{log}} = \frac{\dot{m}_c\ \bar{c}_{p,c}\ \left(T_{c,out} - T_{c,in}\right)}{\frac{\left(T_{h,in} - T_{c,out}\right) - \left(T_{h,out} - T_{c,in}\right)}{\ln \frac{\left(T_{h,in} - T_{c,out}\right)}{\left(T_{h,out} - T_{c,in}\right)}}}. \quad (5)$$

The specific isobaric heat capacity is calculated at the arithmetic mean temperature between inlet and outlet. However, this overall heat transfer coefficient is subject to axial heat conduction within the solid material from the hot end to the cold end, causing the temperature profile of the wall to flatten along the flow direction. This results in smaller cold and higher hot outlet temperatures. This leads to smaller overall heat transfer coefficients than those actually present due to heat transfer when equation (5) is applied directly [25]. Therefore, a direct determination of the heat transfer would lead to correspondingly smaller values as those which are actually present.

3.3. Calculation program for consideration of axial heat conduction

In order to take into account the influence of axial heat conduction, a calculation procedure is set up in Matlab which has already been presented by Fuchs et al. [25]. It is adapted to the heat exchangers used here. A simple program flow schematic of the calculation model is shown in Fig. 7. The inlet temperatures, mass flow rates and inlet pressures are required as input variables. Furthermore, the following geometrical data must be entered for the different heat exchangers: heat transfer area, minimum flow cross-section, hydraulic diameter and the total solid cross-section. These values are derived for a single fin passage directly from the CAD data of the fins. Compared to the data in Fuchs et al. [25], the following deviating definitions have to be considered for the calculation. According to Manglik and Bergles [26], the following applies to the hydraulic diameter

$$d_{h,i} = \frac{4 \cdot A_{f,min,i}}{\frac{A_{ht,i}}{l_i}} \quad (6)$$

where $A_{ht,i}$ is the heat transfer area, $A_{f,min,i}$ is the minimum flow cross section, and l_i is the overflow length of a single fin passage. Based on the number of channels N_i as well as the number of fin passages along $(n_{l,i})$ and across $(n_{t,i})$ to the flow direction, the total heat transfer area as well as the total minimum flow cross-section can be calculated, the following applies for the total heat transfer area

$$A_{ht,tot,i} = N_i \cdot n_{l,i} \cdot n_{t,i} \cdot A_{ht,i} \quad (7)$$

and for the total minimum flow cross section

$$A_{f,min,tot,i} = N_i \cdot n_{t,i} \cdot A_{f,min,i}. \quad (8)$$

The definition of the axial heat resistance coefficient K_p changes to the following expression.

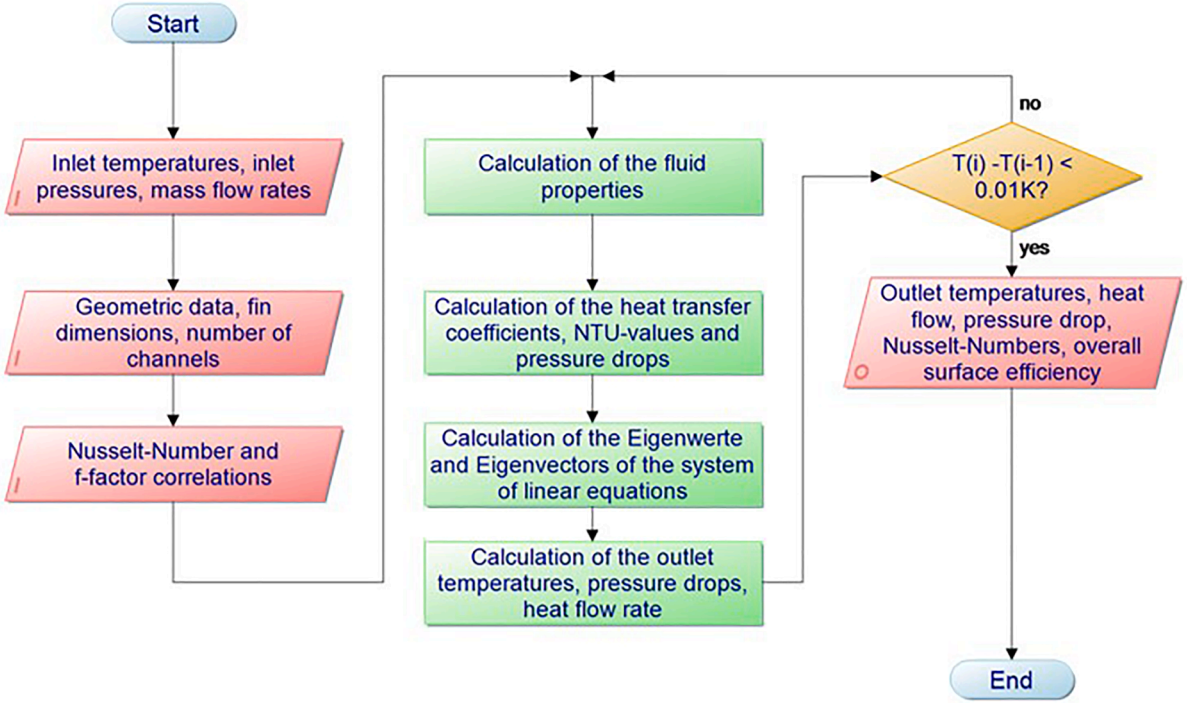

Fig. 7. Program flowchart of the evaluation program to consider axial heat conduction.

$$K_p = \frac{L \cdot (\dot{m} \cdot c_p)_h}{\lambda_s \cdot A_{ax,solid}} \tag{9}$$

with $A_{ax,solid}$ as the solid cross-section (see marked area in Fig. 8). This value is calculated over the entire cross-section of the heat exchanger minus the cross-section of the internal channels (hot and cold sides)

$$A_{ax,solid} = B \cdot H - [(N_c + N_h) \cdot h_{ch} \cdot b_{ch}]. \tag{10}$$

As a third input, correlations matching the heat transferring fins are stored for the calculation of the Nusselt number and the pressure loss coefficient. These can come either from numerical calculations, experiments or literature. For the definition of the heat transfer coefficient in the program, the following still applies

$$\alpha_i = \frac{Nu_i \cdot \lambda_{f,i}}{d_{h,i}}. \tag{11}$$

The overall fin efficiency is calculated using the following equation.

$$\eta_{0,i} = 1 - \frac{A_{fin,i}}{A_i} \left(1 - \eta_{fin,i}\right), \tag{12}$$

where $A_{fin,i}$ describes the heat transferring area of the fins and A_i the total heat transferring area of the hot or cold side. The fin efficiency $\eta_{fin,i}$ is calculated using the well-known equation for planar fins with fin height $h_{f,i}$

$$\eta_{fin,i} = \frac{\tanh\left(m_i \; h_{f,i}\right)}{m_i \; h_{f,i}}, \tag{13}$$

where $m_i = \sqrt{\frac{\alpha_i \; P_i}{\lambda_{fin,i} \; A_i^*}}$. In this equation, P_i denotes the perimeter of a fin, A_i^* its thermally conductive cross-section, and $\lambda_{fin,i}$ the thermal conductivity of the fin material. After the input of the inlet conditions, the geometric data and the correlations for the heat transfer, the calculation of the fluid properties is first calculated at the initial mean temperature

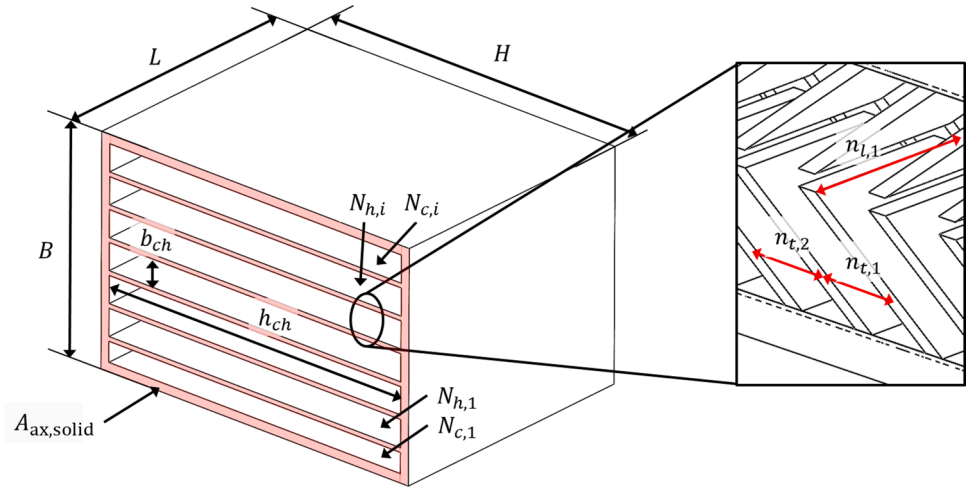

Fig. 8. . Schematic of a heat exchanger section with corresponding dimensions.

$T_m = (T_{h,in} + T_{c,in})/2$. This is followed by the calculation of the heat transfer coefficients (Eq. (11)) and NTU values. The NTU values can now be used to calculate the eigenvectors and eigenvalues of the differential equation system, which in turn are used to solve the equation system (cf. Fuchs et al. [25]). As a result, the outlet temperatures of the heat exchanger are obtained. These new outlet temperatures are used to calculate updated fluid properties and thus heat transfers, the calculation ends when the deviation between two iteration steps is <0.01 K. Output of the calculation are the temperatures, heat flows, pressure losses and Nusselt numbers as well as the overall fin efficiencies. Using the calculated outlet temperatures, the overall heat transfer coefficient is now calculated using Eq. (5). The calculated overall heat transfer coefficient $kA_{cal,j}$ is thus also subject to the axial heat conduction calculated in this case.

3.4. Structure of the correlations for the calculation of the Nusselt number and the Fanning f-factor

The calculation program presented above allows for the calculation of counterflow heat exchangers with different geometries, taking into account the axial heat conduction in the separation plates between the channels as well as in the outer boundary plates. This program will be used to compare the correlations for the Nusselt number and the pressure loss coefficient determined in advance by means of numerical simulations with the measurement results. Furthermore, the calculation program will be modified in such a way as to enable calculation of the experimental Nusselt numbers.

Basically, the correlations for calculating the Nusselt number for offset strip fin structures always conform to the following pattern,

$$Nu_i = C_{Nu,i} \cdot Re_i^{n_{Nu,i}} \cdot Pr_i^{\frac{1}{3}} \cdot \prod_{j=1}^{N} K_{geo,Nu,i,j}^{\gamma_{Nu,i,j}}, \tag{14}$$

as also shown by Manglik and Bergles [26], Joshi & Webb [27], and Chennu [28]. In these, $C_{Nu,i}$ denotes a prefactor describing unspecifiable influences and $n_{Nu,i}$ denotes the exponent of the influence of the Reynolds number on the Nusselt number. $K_{geo,Nu,i,j}^{\gamma_{Nu,i,j}}$ describes the influence of different geometry ratios (index j) on the Nusselt number, for example the ratio of fin height to fin spacing, where each geometry ratio is given its own individual exponent $\gamma_{Nu,i,j}$. However, for the studies undertaken here, the factor $K_{geo,Nu,i,j}$ is set to 1, as the differences in the fin types are caused primarily by their shapes, which cannot be meaningfully expressed by simple geometry ratios. Thus, the simple expression for the hot/cold side (index i=h/c) follows for the Nusselt number

$$Nu_i = C_{Nu,i} \cdot Re_i^{n_{Nu,i}} \cdot Pr_i^{\frac{1}{3}} \tag{15}$$

with the fin type-dependent adjustable parameters $C_{Nu,i}$ and $n_{Nu,i}$.

For the pressure loss coefficient (Fanning f-factor), according to Manglik and Bergles [26], Joshi and Webb [27] and Chennu [28], the following structure follows in a similar way:

$$f_i = C_{f,i} \cdot Re_i^{n_{f,i}} \cdot \prod_{j=1}^{N} K_{geo,f,i,j}^{\gamma_{f,ij}}, \tag{16}$$

as for the case of the Nusselt number, the equation simplifies to the following expression:

$$f_i = C_{f,i} \cdot Re_i^{n_{f,i}}. \tag{17}$$

The corresponding coefficients $C_{Nu,i}$; $n_{Nu,i}$; $C_{f,i}$; $n_{f,i}$ differ with respect to the various fin types presented in the detailed analysis of the heat exchangers.

The development of the fin types presented here was based on shape adjustments to the present flow conditions, as described in the details of the heat exchangers. Based on the numerical calculations, the Nusselt number as well as the Fanning f-factor can be determined for different Reynolds numbers investigated. The Nusselt-numbers can directly calculated by using the fluid and wall temperatures from the numerical calculations, using the definition of the logarithmic temperature difference for constant wall heat flux [29]. For more information on the numerical details of the fin type "Reference", such as validation against literature, determination of the Nusselt number, respectively j- and f-factors and mesh independence, please refer to Fuchs et al. [19] and [30]. The fin types “FO” and "HTO" are based on the fin type "Reference", which is why the calculation mesh used there is used as a starting point and is refined using mesh independence analysis until a mesh-independent result is available. A validation of this calculation takes place in the further course of this article. By logarithmizing the power laws Eq. (15) and (17) and by linear regression, the coefficients $C_{Nu,i}$; $n_{Nu,i}$; $C_{f,i}$; $n_{f,i}$ are fitted to the numerically determined Nusselt numbers and f-factors. The results for the coefficients of the different fin types are shown in Table 2. As the same fin type is installed on the hot and cold side of the heat exchanger, $C_h = C_c$ and $n_h = n_c$ continue to apply to the coefficients of the Nusselt number and f-factor. The temperature-related differences are already covered by the varying Prandtl number and Reynolds numbers.

3.5. Determination of the coefficients C_{Nu} and n_{Nu} from the experimental data

As with the numerical calculations, pressure loss coefficients and, in particular, Nusselt numbers are to be obtained from the experimental data in order to be able to better compare the agreement of the numerical calculations with the experiments rather than to restrict oneself to the overall heat transfer coefficients alone. The determination of the coefficients C_f and n_f is quite straight forward. By logarithmizing the power law (Eq. (17) and by performing a linear regression over all measuring points of the f-factor (calculated according to Eq. (4)), these can be determined for the three (six) different fin types (heat exchangers).

The determination of the coefficients for the Nusselt number is to be done on the basis of the measured overall heat transfer coefficients. For this purpose, the presented calculation program is slightly modified and used to calculate heat transfer coefficients that are already subject to axial heat conduction. The coefficients C_{Nu} and n_{Nu} obtained from the experiments are shown in the results chapter. Arbitrary starting values for the coefficients C_{Nu} and n_{Nu} are given to the calculation program and a corresponding overall heat transfer coefficient is calculated. The calculated overall heat transfer coefficients are then compared with the experimental data. The coefficients C_{Nu} and n_{Nu} are then varied until the deviation between the calculated and experimental overall heat transfer coefficients is minimal. This results in a nonlinear optimization problem for the determination of the unknown coefficients in Nusselt correlations, as also presented by Rose [31], Khartabil and Christensen [32] and Steinhoff [33]. This optimization problem can be expressed by the following equation.

$$s = \min_{\vec{x}=(C_{Nu},n_{Nu})} \left(\sqrt{\frac{1}{N_{test}-1} \sum_{j=1}^{N_{test}} \left(1 - \frac{kA_{exp,j}}{kA_{cal,j}(\vec{x})}\right)^2} \right), \tag{18}$$

where the index j represents each individual measuring point and N_{test}

Table 2
Coefficients for the Nusselt- and f-factor correlations obtained from the numerical simulations.

Coefficients	Ref	FO	HTO
C_{Nu}	0.961	0.747	0.653
n_{Nu}	0.39	0.399	0.412
C_f	5.55	5.68	5.49
n_f	−0.672	−0.697	−0.688

the maximum number of measuring points used for optimization. $kA_{exp,j}$ denotes the respective experimental overall heat transfer coefficient and $kA_{cal,j}$ an overall heat transfer coefficient calculated by means of the program, depending on the selected parameters C_{Nu} and n_{Nu}. For the optimization, a *genetic algorithm* is used to determine the global minimum and not a possible local one, Matlab R2021b [34] is used as the calculation program. For the algorithm, a starting population of 10,000 individuals is used and the number of generations is set to 5000, thus achieving an accurate exploration of the solution space [35]. The recommended settings of Matlab are used for the mutations and inheritances. Following the optimization by means of the genetic algorithm, the global minimum is further narrowed down via the local algorithm *fmincon* in order to determine the exact coefficients C_{Nu} and n_{Nu}. The choice of the measurement points for the evaluation is crucial for the result of the optimization. The parameters C_{Nu} and n_{Nu} for the calculation of the Nusselt number should only be influenced by convection. Therefore, only the measuring points of the temperature level 200/80°C are used for the determination of the parameters C_{Nu} and n_{Nu} in order to keep the influence of potential heat radiation as low as possible. The influence of axial heat conduction is already taken into account via the model. With the coefficients determined in this way, the Nusselt numbers for the two other temperature levels at 400/80°C and 700/380°C can also be calculated and the resulting overall heat transfer coefficients compared with the experimental data. The comparison provides information on the extent to which additional heat-transfer effects, such as heat radiation, occur in the measurements which may influence the results.

3.6. Determination of the measurement uncertainty

The determination of the measurement uncertainty is basically carried out according to the "Guide to the expression of Uncertainty in Measurement" [36]. The uncertainties of the measuring equipment used as well as the correlations for the calculation of the fluid properties are summarized in Table 3. The uncertainties of the geometric parameters are not considered. The calculation of the measurement uncertainties of overall heat transfer coefficient, f-factor, Reynolds number and other directly derivable quantities can be calculated directly via the error propagation. The calculation of the uncertainties of the heat transfer coefficients, or the Nusselt number, on the other hand, must be done by a different method, since their uncertainties depend not only on the Reynolds number, but also on the coefficients C_{Nu} and n_{Nu}, which must be determined [37]. For this purpose, 100,000 random start values for the optimization are distributed in the solution space and, using a MonteCarlo-like method programmed in Matlab, the solution range of the coefficients C_{Nu} and n_{Nu} is calculated in such a way that the resulting uncertainties of the calculated overall heat transfer coefficients correspond to the uncertainties of the measured overall heat transfer coefficients. The principle is also shown in Fig. 9. With this procedure, the uncertainties of the calculated coefficients C_{Nu} and n_{Nu} and consequently the one of the Nusselt numbers are determined.

Table 3
Uncertainty parameters, their assumed distribution function and the deviation.

Parameter	Distribution function	Deviation
Temperature	rectangular	$\pm 0.002 \cdot \vartheta$
Volume flow hot side	rectangular	±0.5 % rd. ± 0.1 % FS
Volume flow cold side	rectangular	±1.5 % rd. ± 0.3 % FS
Height difference in U-tube manometer	rectangular	±1 mm
Specific isobaric heat capacity [40]	rectangular	±0.3 %
Thermal conductivity [41]	rectangular	±2 %
Dynamic viscosity [23]	rectangular	±4 %

4. Evaluation of the experiments

4.1. Validation of the optimization algorithm

The proper functioning of the optimization algorithm is validated in advance using numerical flow simulations for the "Reference" fin type. Based on the numerically determined fluid and wall temperatures given in Fuchs et al. [19], the Nusselt numbers are determined for different Reynolds numbers and a correlation according to equation(15) is derived. This is implemented in the design program and a calculation of different operating points (with and without axial heat conduction) with different mass flow rates and temperatures is performed. The overall heat transfer coefficients determined in this way are in turn used as a starting point for the optimization in order to determine the corresponding coefficients C_{Nu} and n_{Nu} via the algorithm. As a result, both without and with consideration of axial heat conduction, the identical coefficients are determined on two decimal places as in the numerical calculation, thus confirming the basic function of the optimization algorithm. The results are shown in Table 4.

4.2. Evaluation of the overall heat transfer coefficients for the different heat exchangers

The determination of the coefficients C_{Nu} and n_{Nu} is performed on the basis of the measurements at the 200/80°C temperature level. Due to the low temperature level, further internal heat transfer effects, especially radiation, can be minimized or excluded. Furthermore, the heat losses are significantly lower and thus they influence the measured overall heat transfer coefficients to a much lesser extent. Before the overall heat transfer coefficients are presented, a brief review of the test rig performance will first be made. For this purpose, Fig. 10 shows the parity plots of the heat flows for the hot and cold sides for the three temperature levels, exemplarily for the fin type "HTO" vers. 2. The figure shows that the energy balances differ between 3.5 and 10% for all three temperature levels, except for very low Reynolds numbers for the 700/380°C measurement. However, a slight systematic error can also be observed, this is due to insufficient mixing of the hot outlet in this heat exchanger, whereby as the mass flow rate increases, a hot air strand distorts the result and therefore the hot outlet temperature turns out to be between 1-4K higher. For the other heat exchangers, the mixing chamber was revised accordingly so that this error no longer occurs for these heat exchangers. The determined measurement data can therefore be used for further evaluation. Fig. 11 shows the parity plots of the overall heat transfer coefficients for the different heat exchangers, the different colours symbolize the different temperature levels. The overall heat transfer coefficients are also corrected for heat losses by adjusting the outlet temperature of the hot side accordingly. The x-axis represents the experimentally determined overall heat transfer coefficient and the y-axis the overall heat transfer coefficient calculated by means of the optimization algorithm.

The comparison clarifies several aspects. The selected ansatz function is very well suited to describe the Nusselt numbers for all heat exchangers investigated, both in the Vers. 1 and Vers. 2 at the 200/80°C temperature level. The average deviation from the parity line for all heat exchangers is only 0.1% and the maximum deviation is 2%. Table 5 summarizes the experimental coefficients C_{Nu} and n_{Nu} for the different fin types and versions and the respective intervals (95.4% confidence interval). If the coefficients C_{Nu} and n_{Nu} determined at the 200/80°C measurement are used to calculate heat transfer coefficients at the higher temperature levels, a similar picture emerges. Here, the deviations increase for the 400°C measurements, with no systematic deviation in the positive or negative direction for any heat exchanger. From this it can be concluded that for the 400°C measurements there are apparently no additional heat transfer effects, such as internal heat radiation, which would lead to a significant systematic deviation of the overall heat transfer coefficient compared to the 200°C measurements.

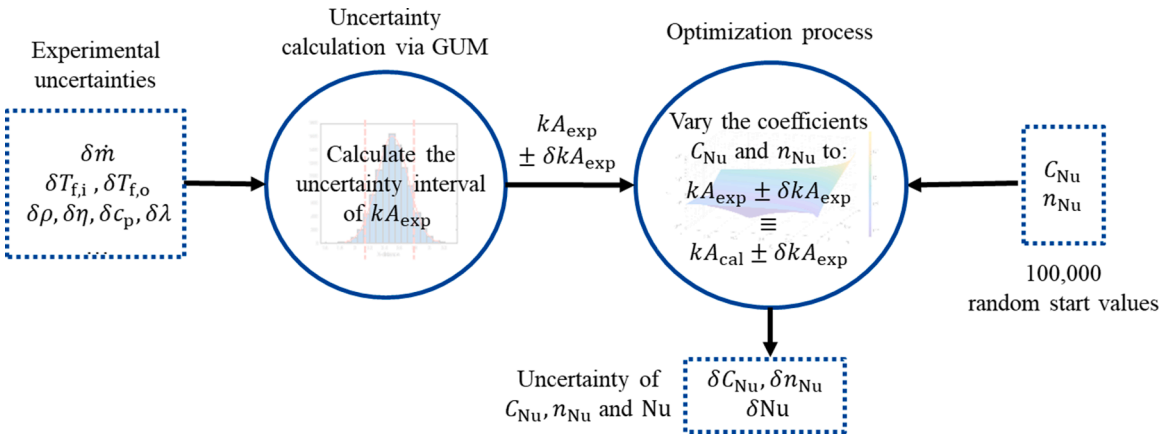

Fig. 9. Flow chart of the uncertainty calculation principle for C_{Nu} and n_{Nu}.

Table 4
Comparison of the coefficients C_{Nu} and n_{Nu} from the numerical calculation and the optimisation procedure.

	C_{Nu}	n_{Nu}
Numerical	0.9612	0.389
Opt. with axe. heat conduction	0.9605	0.3892
Opt. without axe. heat conduction	0.9605	0.3892

Furthermore, the comparison shows that the calculation of the axial heat conduction is performed correctly and depicts the influence adequately. In the 700°C measurements, systematic deviations now occur in isolated cases for the respective heat exchangers, although these are not limited to systematic higher or lower overall heat transfer coefficients compared to the parity line. The heat exchanger "Reference Vers. 2" shows increasingly higher experimental overall heat transfer coefficients (max. +6.7%) for increasing Reynolds numbers. The other heat exchangers with similar internal fin type show smaller experimental overall heat transfer coefficients. However, an analysis of the measurement uncertainties also shows that this has increased significantly for the 700°C measurements and that the measurement points of all heat exchangers also extend beyond the parity line. The reasons for these increased uncertainties lie in the increased uncertainty of the temperature measurement due to thermal radiation, which is added to the already higher sensor-related uncertainty at high temperatures. A more detailed analysis of this temperature level follows in the further course of this article.

In summary, for all heat exchangers investigated and furthermore for all three temperature levels investigated, the maximum deviation of the overall heat transfer coefficients excluding the two extreme points is less than 15%. The corresponding percentage errors for all heat exchangers are summarized in Table 6.

4.3. *Detailed investigation of the Nusselt-Number and the Fanning f-factor*

With the C and n values determined for the various heat exchangers, it is now possible to determine the Nusselt numbers for the Reynolds numbers at 200/80°C as well as at 400/80°C and 700/380°C. Furthermore, a comparison between the versions 1 and 2 can be made and how the fin configurations affect the Nusselt numbers and the f-factor.

For the heat exchangers "Reference" vers. 1 and vers. 2, the experimental and numerical Nusselt numbers and the f-factors are shown in Fig. 12. The evaluation of the Nusselt number and f-factor shows that the agreement between the experiments and the simulation for version 2 can be described as good over the entire Reynolds number range. The deviation of the Nusselt number is less than 4% for average Reynolds-numbers ($Re \approx 300$) and a maximum of 11% for high Reynolds numbers ($Re \approx 580$). The measurement uncertainty of the Nusselt-number ranges between ±6.6 % at $Re \approx 580$ and ±12.5 % at $Re \approx 100$. The relative uncertainty is decreasing with increasing Reynolds

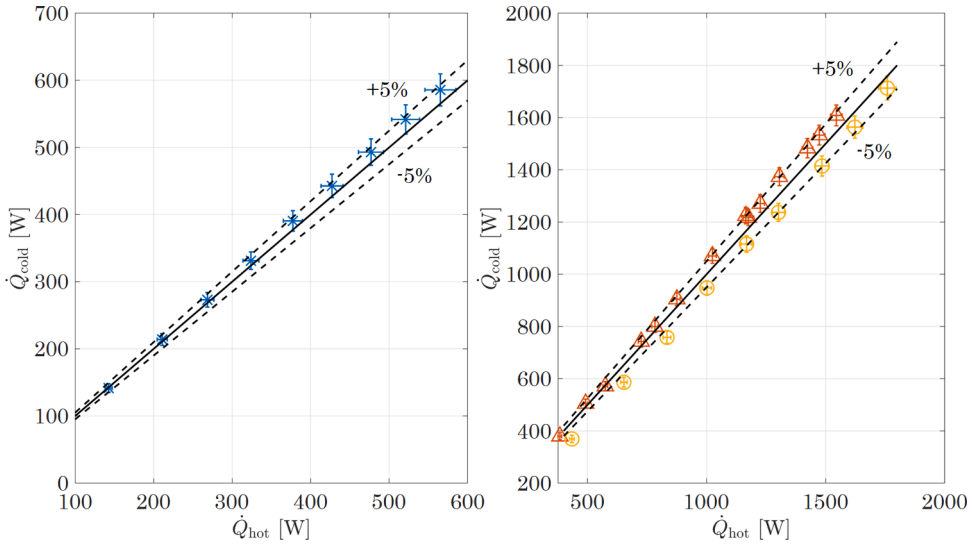

Fig. 10. Parity plot of the heat flows for: left: 200/80 °C measures, right: 400/80 °C and 700/380 °C measurements.

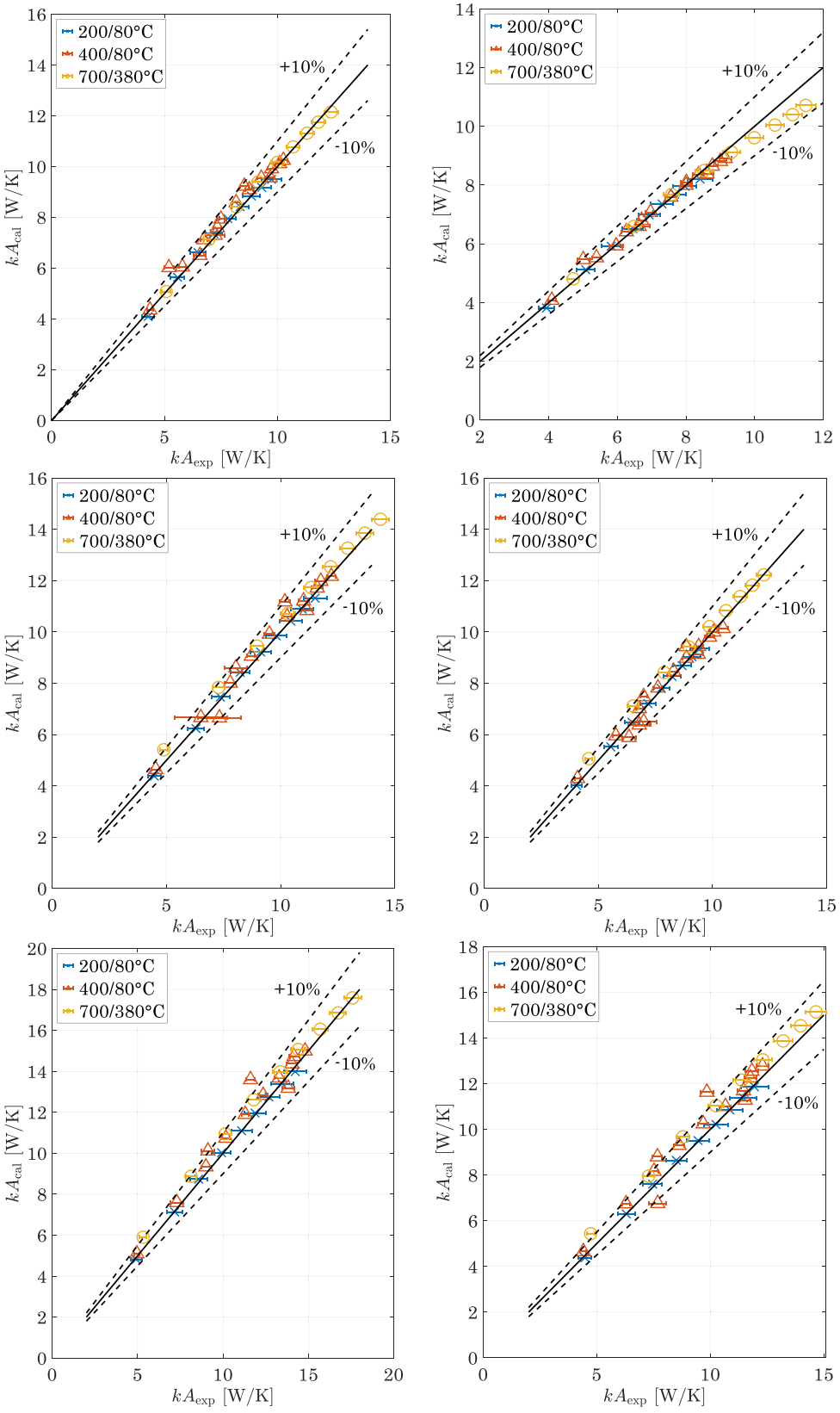

Fig. 11. Parity plots of the overall heat transfer coefficient of the three different fin types in version 1 and 2
top: "Reference (Ref)" left: version 1, right: version 2 middle: "Flow optimized (FO)" left: version 1, right: version 2 bottom: "Heat Transfer Optimized (HTO)" left: version 1, right: version 2.

Table 5
Coefficients for C_{Nu} and n_{Nu} and their absolute uncertainty range (95,4% confidence interval, $z = 2$).

Fin type	Version	Coefficients	Uncertainty range (95,4%)
Ref	1	C_{Nu} : 1.408	(1.060, 1.879)
		n_{Nu} : 0.347	(0.312, 0.381)
	2	C_{Nu} : 1.441	(1.125, 1.845)
		n_{Nu} : 0.309	(0.279, 0.337)
FO	1	C_{Nu} : 1.01	(0.735, 1.389)
		n_{Nu} : 0.386	(0.345, 0.426)
	2	C_{Nu} : 1.065	(0.813, 1.386)
		n_{Nu} : 0.334	(0.302, 0.366)
HTO	1	C_{Nu} : 0.793	(0.548, 1.151)
		n_{Nu} : 0.417	(0.369, 0.465)
	2	C_{Nu} : 0.674	(0.497, 0.913)
		n_{Nu} : 0.405	(0.367, 0.443)

Table 6
Minimum, maximum and mean errors of the overall heat transfer coefficients for each fin type and version.

	Ref vers. 1	Ref vers. 2	FO vers. 1	FO vers. 2	HTO vers. 1	HTO vers. 2
Min. error [%]	0.002	0.039	0.097	0.192	0.005	0.07
Max. error [%]	19.51	12.57	30.64	31.17	36.78	37.44
Mean error [%]	3.43	2.65	4.52	4.42	5.57	7.39

number, since the uncertainty of the overall heat transfer coefficient is also decreasing with increasing Reynolds-number. Due to the decreasing effectiveness of the heat exchanger as the Reynolds number increases, the uncertainties of the temperature measurement have less influence on the determination of the overall heat transfer coefficient and thus on the underlying Nusselt numbers. This fact applies to all heat exchangers and versions studied here.

The deviation between simulation and measurement thus correspond to the values determined by Chennu [28] and [38] in his calculations for off-set strip fin heat exchangers in the laminar region. The analysis of the f-factor shows a scatter of about ±5 % due to the direct evaluation of measured data, nevertheless the agreement with the numerical data over the whole Reynolds number range can also be considered as good. The measured data of all temperature levels are on average 8% higher than the simulation data, while no systematic differences between the hot and cold side can be determined. The analysis of the uncertainty of the f-factor shows a similar behaviour, with increasing Reynolds-number the uncertainty of the f-factor is reduced. The uncertainty of the f-factor ranges between ±4.4 % at Re ≈ 580 and ±19.1 % at Re ≈ 100. Due to the higher pressure drop at higher Reynolds-numbers the error in reading has less impact on the overall pressure drop and therefore on the calculated f-factor, leading to smaller errors. It should be noted that only a limited number of uncertainty bars are shown for the f-factor as well as for the Nusselt number, as otherwise the readability of the diagrams suffers considerably. The uncertainties of the measurement points without error bars can be estimated from the adjacent error values, because of the constant trend from low to high Reynolds-numbers.

When the measurement uncertainty is taken into account, for small Reynolds numbers the simulation data are within the uncertainty range of the measured data. A comparison with literature data shows comparable deviations for the f-factor. In general, it can be stated on the basis of literature data that the f-factors are usually subject to greater scatter than the heat transfer values, as is also the case here. Furthermore, this analysis shows that the significantly increased roughness of the additively manufactured heat exchangers apparently has only a minor influence on the pressure losses, as is also to be expected with laminar flow [23,29]. The hypothesis stated in some publications [16, 11] that roughness leads to higher friction coefficients even in laminar flows cannot be confirmed here. However, it should be pointed out that, especially for small channels with $d_h < 1$ mm, the existing roughness typically leads to a reduced hydraulic diameter and thus to increasing friction coefficients. This makes it increasingly difficult to clearly distinguish between roughness-driven effects and simple flow acceleration by smaller hydraulic diameters.

The evaluation of the Nusselt number of the "Reference" version 1 heat exchanger results in deviations of +10 % – +20 % compared to the numerical data, with measurement uncertainties between ±6.7 % – 13.9 %. However, due to the systematically higher heat transfers, a corresponding influence of the bulge on the fin tips cannot excluded. As a result of the structure on the fin tips and the resulting smaller channel centre (see Fig. 3), the fluid is forced into the area of the fin flanks, which results in improved heat transfer there due to thinner thermal boundary layers. A comparison of the calculated and experimental overall heat transfer coefficients shows that also the 400/80°C and 700/380°C measurements can be well correlated by the coefficients C_{Nu} and n_{Nu} determined at 200/80°C. Therefore, correspondingly higher Nusselt numbers as in the simulation are also obtained at these two temperature

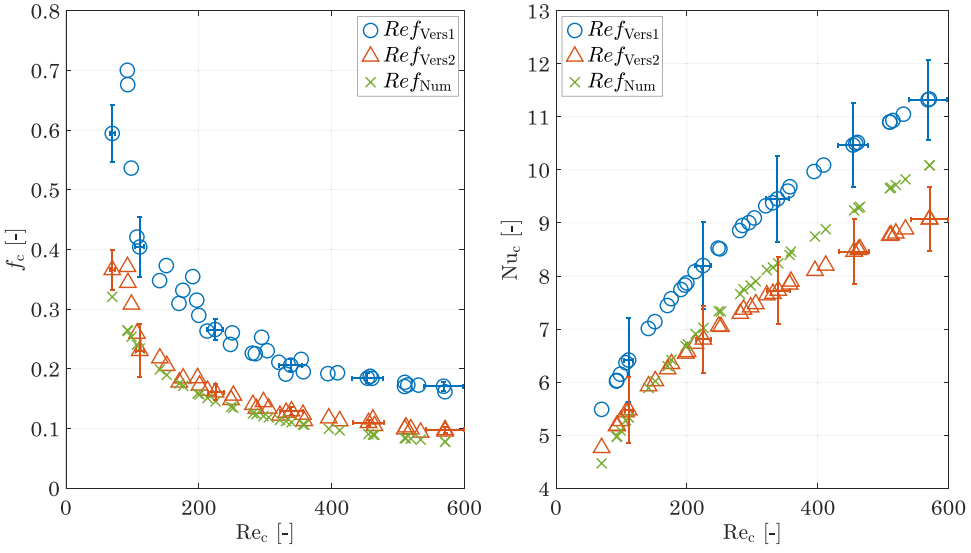

Fig. 12. Fanning f-factor and Nusselt-Number for "Reference" (Ref) in Version 1,2 and numerical values on the cold side.

levels.

An analysis of the f-factors of "Reference" version 1 shows an increase of about 40% compared to the numerically determined values. This is to be expected due to the reduced flow cross-section as a result of the fin structures. The flow is forced in the direction of the fin flanks, resulting in greater frictional pressure losses due to the thinner hydrodynamic boundary layer.

Fig. 13 shows the Nusselt numbers and the f-factors for the heat exchangers "FO" version 1 and version 2, as well as the numerically determined data for the corresponding fin type. The fin type used is a flow-matched shape, where the fins are shaped according to the streamlines. The analysis of the Nusselt number also shows an overestimation of the numerical data of about 20% for version 1. The f-factors of the experiments exceed the simulation data by 40%. For both deviations, it is again assumed that they are caused by the fin structures, which, as in the case of the heat exchanger "Reference" Version 1, lead to a shift of the fluid from the center of the channel towards the fin flank and thus increase heat transfer and pressure drop. The heat exchanger "FO" version 2 shows a very good agreement between the experimental and numerical values of the Nusselt number over the whole Reynolds number range. The deviation is approx. +3% for small Reynolds numbers and approx. -2% for larger Reynolds numbers and is thus within the range of the measurement uncertainty, which is approx. $\pm$ 6.5 % – 12.2 % as before. The f-factor also shows good agreement, with the experimental data being about 10% higher than the numerically determined values throughout the Reynolds number range. There is still a larger scatter of the measured data, but this is also due to the reading accuracy, especially for the smaller Reynolds numbers, as indicated by the error bars. As already was the case for "Reference" version 2, the very small adjustments at the tip of the fin leads to a clear improvement and should therefore always be taken into consideration.

Fig. 14 shows the calculated as well as the experimental derived Nusselt numbers and the f-factors for the heat exchangers "HTO" version 1 and version 2. As with the two previous heat exchangers, version 1 also shows a Nusselt number that is approx. 23 – 26 % higher than in the simulation and f-factor that is approx. 120% higher. As with the two previous versions 1, the reduction in cross-section due to the fin assemblies is cited to be the cause. For version 2, there is again much better agreement between the Nusselt numbers and the f-factor. The experimental Nusselt numbers differ from the numerically calculated data by only 1%. For the f-factor of the hot and cold side, about 9% higher values are determined in the experiments, the scattering of the f-factors corresponds to that of the other heat exchangers investigated. The uncertainties of the f-factor are smaller for low Reynolds-numbers compared to the other heat exchanger, since this type of fin has the overall highest pressure drops. The uncertainty in the Nusselt-number is of the same magnitude as for the other fin types.

To illustrate the differences between versions 1 and 2, the ratios of the Nusselt numbers and f-factors of the cold side between versions 1 and 2 are shown in Fig. 15. On the hot side the results are the same. For the reference fin type, there is a moderate dependence of the Nusselt number ratio on the Reynolds number. The ratio increases from about 1.15 to 1.25 for the highest Reynolds number. The f-factor ratio reacts less sensitively to a change in the Reynolds number, falling from just under 1.75 to 1.69. For the fin type "Flow Optimized" a stronger dependence can be observed, the Nusselt number ratio increases for increasing Reynolds numbers from 1.17 to just over 1.30. Likewise, the f-factor shows a stronger decrease from 1.90 to 1.75. For the "heat transfer optimized" fin type, the smallest dependence of the Nusselt number ratio between version 1 and version 2 on the Reynolds number is obtained, ranging from 1.23 to 1.265. For the f-factor ratio there is even almost no dependence on the Reynolds number, it stays relatively constant showing an increase between 2.22 and 2.225. In particular, the fin type "HTO" with the smallest hydraulic diameter shows almost no flow-dependent effects (quasi-constant value of the relative f-factor). This suggests that the variations in f-factor between version 1 and version 2 are caused by a fixed change in geometry and thus a change in hydraulic diameter. Slightly larger changes in relative f-factor are observed for the reference fin type, so increasing velocity-dependent flow effects are occurring. However, a laminar/turbulent transition point, typically expressed by a kink in the course of the f-factor (and the Nu number), cannot be determined. For the "FO" fin type, both the relative Nusselt number and the relative f-factor give the largest dependencies on the Reynolds number. This is possibly due to the shape of the fin, which has a decreasing thickness in the flow direction, so that an increasingly larger detachment area occurs with increasing Reynolds number. The manufacturing inaccuracies present in version 1 push the flow in the direction of the fin flank, so that this detachment effect is intensified and leads to a stronger Reynolds dependence of the f-factor and the Nusselt number.

4.4. Interim conclusion on the difference between version 1 and version 2

The previous investigations show that the slight modification at the fin tip leads to a significant improvement in the predictability of the heat transfer and pressure drop for all three heat exchanger fin types

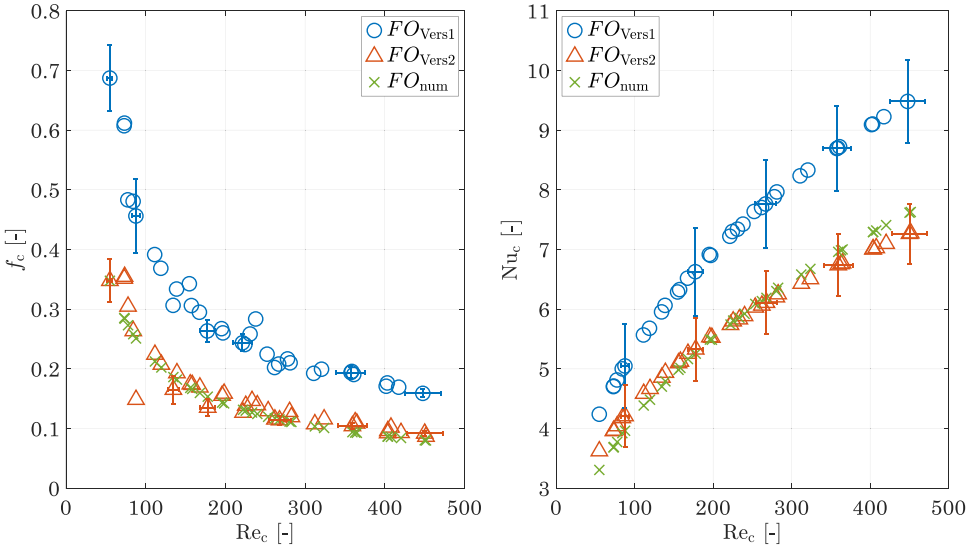

Fig. 13. Fanning f-factor and Nusselt-Number for "FO" in Version 1,2 and numerical values on the cold side.

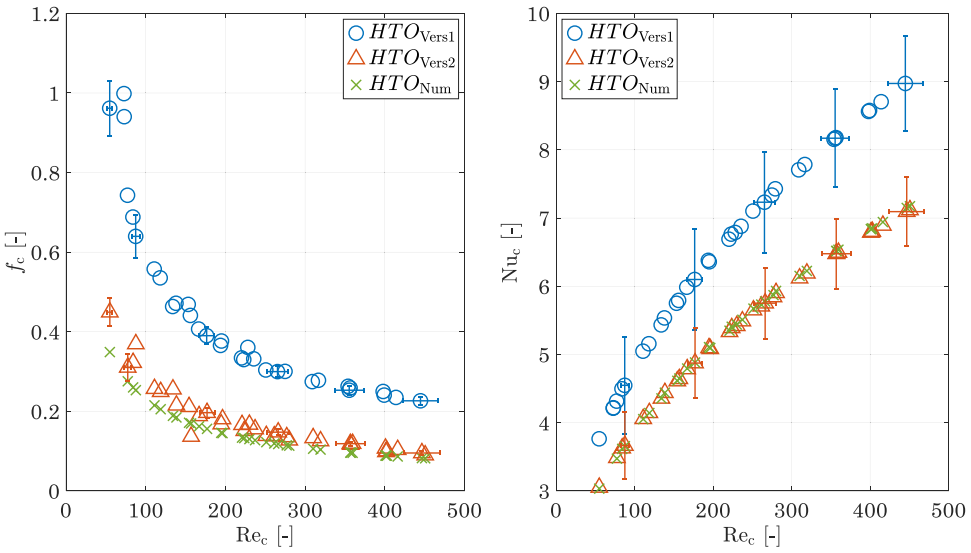

Fig. 14. Fanning f-factor and Nusselt-Number for "HTO" in Version 1,2 and numerical values on the cold side.

investigated. Furthermore, the investigations confirm that geometry adjustments in the submillimetre range are possible by means of additive manufacturing and that these adjustments are metrologically seen in the heat transfer and pressure drop. This opens up the possibility that only small adjustments need to be made to the fin types for targeted optimization of heat transfer and pressure drop, which nevertheless have a correspondingly large effect. Additionally the main contributor to the deviations between numerical and experimental values are manufacturing inaccuracies, resulting in differences in the hydraulic diameter. The surface roughness is only of minor importance in the laminar flow region.

4.5. Comparison of the fin types in version 2

The heat exchangers examined here all have the identical external and channel dimensions, they differ only with regard to the internal fin types. These fin types have been optimized for heat transfer and pressure drop behaviour, as already mentioned in the detail heat exchanger analysis in section 2. Therefore, a direct comparison of the version 2 fin types will be made again here. Fig. 16 shows the experimentally determined Nusselt numbers and f-factors of all three temperature levels for the three fin types. Only the cold side is considered, the results for the hot side are analogous. The comparison shows that for higher Reynolds numbers, the "Reference" fin type exhibits approx. 15 −20 % higher f-factors than the optimized "HTO" and "FO" fin types. The latter two fin types show almost identical f-factors at higher Reynolds numbers. For lower Reynolds numbers, the "Reference" and "HTO" fin types exhibit nearly identical f-factors, while the "FO" fin type tends to yield smaller f-factors. However, the measurement uncertainty is also greatest for small Reynolds numbers due to the increasing reading inaccuracy, which is why no clear differentiation can be made. Overall, all three fin types show very similar f-factor levels. If the Nusselt number in Fig. 16 (right) is considered, clearer differences between the fin types become apparent. The "Reference" fin type gives the highest Nusselt numbers in the entire Reynolds number range studied, these being about 20% above the values of the "FO" fin type and between 20 − 38 % above the values of the "HTO" fin type. The Nusselt numbers of the fin type "FO" are between "HTO" and "Reference" at small Reynolds numbers, but show a slightly decreasing tendency with increasing Reynolds number and approach the values of the fin type "HTO". The result is initially surprising, since the "FO" and "HTO" fin types were developed towards an increased heat transfer, with the focus on a thin thermal boundary layer in the case of fin type "HTO" in particular. Here, however, evaluation on the basis of the Nusselt number falls short of the mark. If geometry optimization is carried out with a focus on a thin boundary layer, this also leads to a smaller hydraulic diameter in the cases considered here. However, this decrease in hydraulic diameter is greater than the increase in the corresponding heat transfer coefficient due to the thinner thermal boundary layer. This ultimately results in smaller Nusselt numbers for actually optimized fin types, although higher heat transfer coefficients are present. Fig. 17 below shows the heat transfer coefficients of all temperature levels in relation to the respective average thermal conductivity of the fluid. This ratio is in turn proportional to the thermal boundary layer thickness [29], so

$$\frac{\alpha}{\lambda} \propto \frac{1}{\delta_t}. \tag{19}$$

It holds true that the curves shown in Fig. 17 represent the reciprocal of the thermal boundary layer thickness. This clearly shows that the "HTO" fin type has the thinnest thermal boundary layer thickness, especially for higher Reynolds numbers, as was the aim of optimizing this fin type and as would be expected from the shape of the fin types. In comparison, the "FO" fin type shows the thickest thermal boundary layer thickness on average, which is also to be expected on the basis of the optimization objective mentioned at the beginning with regard to a lower pressure drop. The "Reference" fin type is located between the two other fin types, with even slightly thinner boundary layers for low Reynolds numbers than for "HTO". However, the measurement uncertainty in these ranges is higher and the results are closer together, so that incorrect measurements cannot be ruled out. Another important aspect in differentiating between the various optimization measures is the surface efficiency of the fin types, which is shown in Fig. 17, right. Here, the basic fin type "Reference" shows the lowest surface efficiency, which ranges between 0.615 and 0.765. The fin type "FO" ranks on average 5% above the basic fin type, which is primarily achieved by the enlarged fin cross-section in the inflow area. The "HTO" fin type achieves surface efficiencies approx. 8 − 9 % higher than the basic fin type and is thus the most efficient.

4.6. Evaluation of a potential radiation influence

The different temperature levels have been chosen to increase the range of the Reynolds number, but also to investigate the influence of heat radiation. The transmitted radiant heat flux depends on the fourth power of the thermodynamic temperatures involved. The influence of thermal radiation manifests itself in the heat exchangers in two ways.

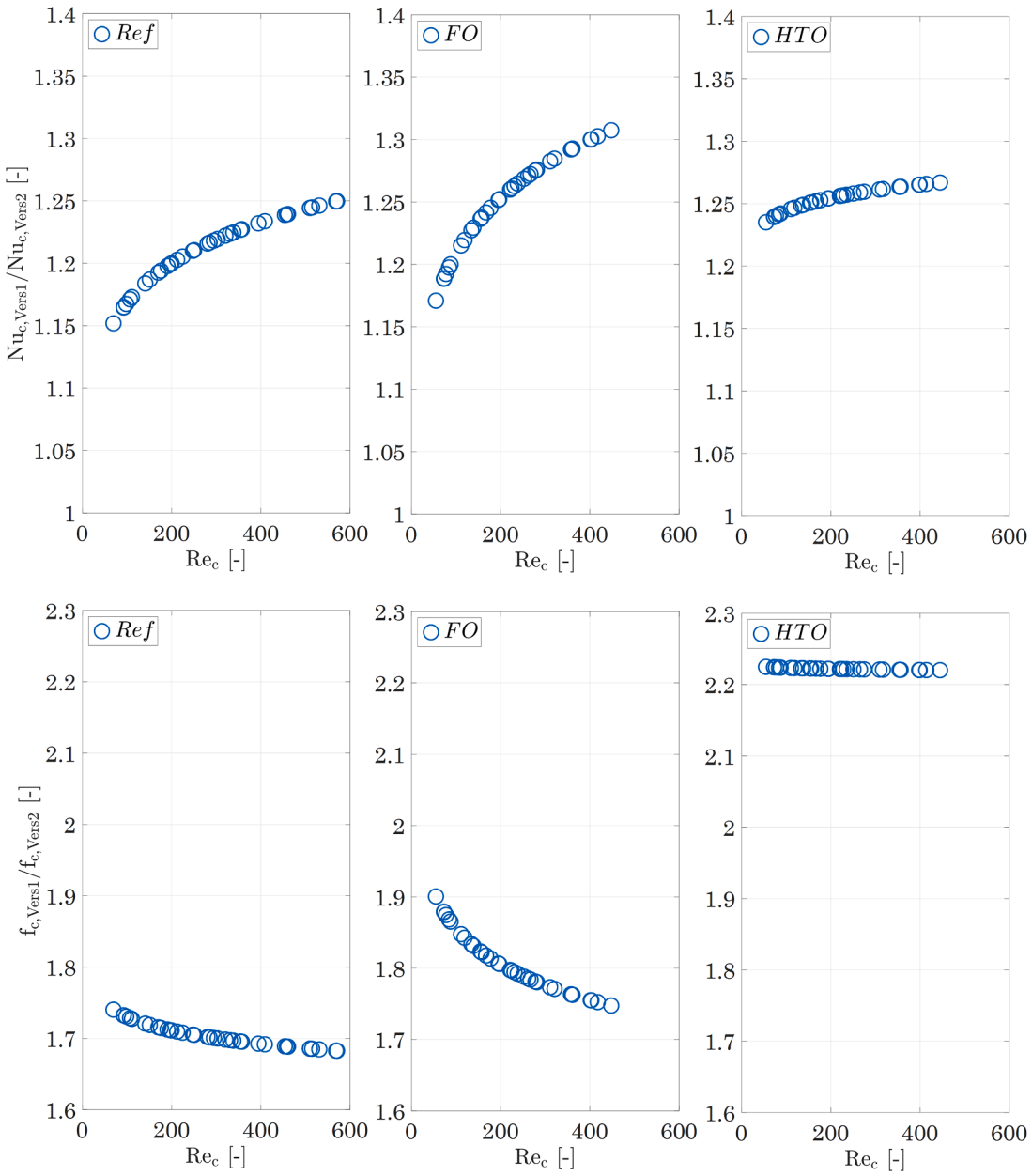

Fig. 15. Top: ratio of the Nusselt-number (version 1/version 2) for each fin type on the cold side, Bottom: Ratio of the f-factor (version 1/version 2) for each fin type on the cold side.

First, the radiant heat occurs between the fin tip and the fin root, thus providing an additional heat flux in addition to the heat conduction through the fin material, which results in a higher performance of the heat exchanger. The course of the radiant heat flux is inversely proportional to the fin efficiency; if the latter increases, the heat flux transmitted by radiation decreases, and vice versa. On the other hand, the thermal radiation also leads to a radiation exchange in the axial direction of the heat exchanger and thus to a shift of the temperature profile, which leads to a reduction of the efficiency similar to the axial heat conduction in the solid [25]. For the investigation of the radiation influence, a comparison of the overall heat transfer coefficients is resorted to for the different heat exchangers. As mentioned at the beginning, only the measurements at 200/80°C are used for the evaluation of the Nusselt numbers for the heat exchangers. The Nusselt numbers determined in this way are now used to calculate the overall heat transfer coefficients at the 700/380°C measurements (also already shown in Fig. 11). By comparing the calculated data with the experimentally determined data at 700/380°C, the differences from the 200/80°C measurements can thus be determined. The increased heat losses have already been calculated out of the overall heat transfer coefficients presented at the beginning, so that the differences are finally caused to a significant extent by thermal radiation. Fig. 18 shows the curves of the overall heat transfer coefficients for the three fin types of version 2 at the two temperature levels. For all three fin types, the agreement between the calculated and experimentally determined overall heat transfer coefficients is ≥ 91 % and thus within the range of measurement uncertainty. For the fin type "Reference" a Reynolds number dependence is shown. For small Reynolds numbers $30 < Re < 150$, there is very good agreement with the model data. If the Reynolds number is increased, the deviation in favour of the experimental values increases to 3%. This is determined by the course of the fin efficiencies, which decrease with increasing Reynolds number. As a result, the temperature difference between the fin tip and the fin root increases and the radiant heat flux increases. Furthermore, it apparently

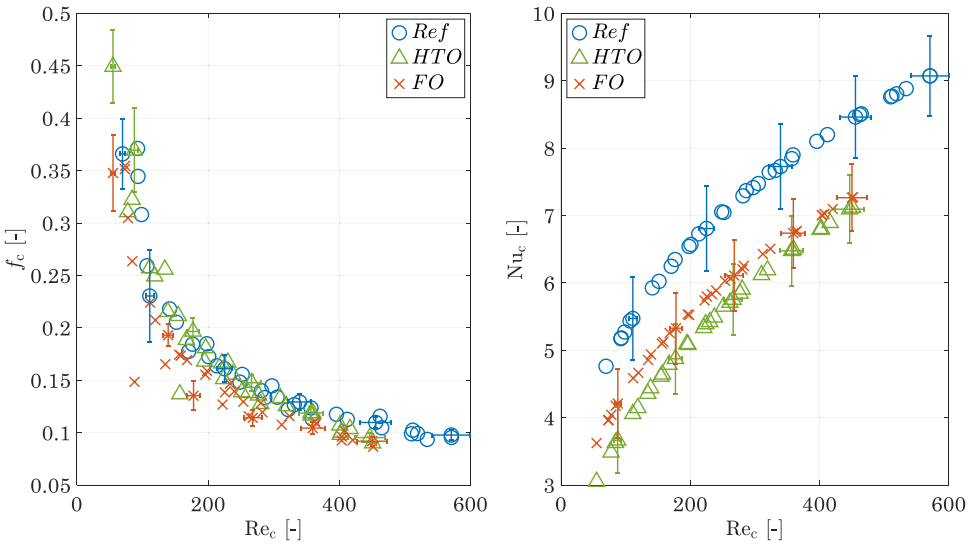

Fig. 16. f-factor and Nusselt-Number of each fin type in Version 2 on the cold side.

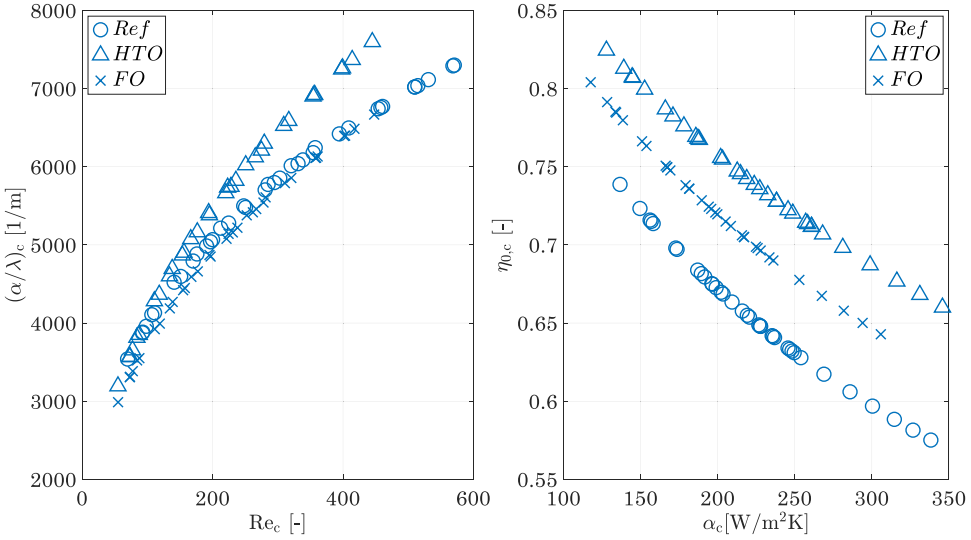

Fig. 17. Inversed thermal boundary layer thickness and surface efficiency for each fin type in Version 2 on the cold side.

outweighs the axial radiant heat flux and thus leads to a slightly increased performance of the heat exchanger. For the fin type "FO", slightly different results are obtained. Here, only a slight deviation of <3% in favour of the model data is shown over the entire Reynolds number range, but larger measurement uncertainties are also present. The "FO" fin type thus shows an increased negative influence of thermal radiation. This may well be due to the shape of the fins. These exhibit a qualitatively larger view factor in the direction of the lower temperatures, which increases the radiant heat flux in the axial direction, while the view factor transverse to the flow direction remains almost unchanged. Despite this negative influence, the fin type "FO" leads to a higher overall heat transfer coefficient than the fin type "Reference" for the 700/380°C measurements. For the fin type "HTO", the largest deviation between the model and the experimental data results with approx. 5% in comparison. It is noticeable that the deviation from the model becomes smaller as the Reynolds number increases. As with the previous fin types, this can be explained by a decreasing fin efficiency and thus an increasing radiation heat flux transverse to the flow direction. The radiation in the flow direction (quasi-axial heat conduction) is favoured by the decreased fin efficiency, but the higher flow velocity provides a smaller temperature gradient along the separation plate between the fluids and reduces not only the axial heat conduction in the solid but also the radiation heat flux in the axial direction, which leads to a better agreement between model and experiment. The analysis of the influence of the high temperature levels on the performance of the different heat exchangers shows a slightly negative influence of thermal radiation, especially at low velocities. The heat transfer coefficients are calculated between 3 and 8% too high, depending on the fin type. When the Reynolds numbers are increased, thermal radiation leads to a higher overall heat transfer coefficient of 3% for the "Reference" fin type, similar results were found by Luo et al. [39]. A slight decrease between 1 and 3% is observed for the other two fin types. This is most likely due to the higher fin efficiency of the two optimized fin types, which leads to a lower positive influence of the thermal radiation, while the "axial" thermal radiation can still play out its negative influence, which is favoured by the increased view factor due to the shaping of the fin types.

5. Conclusion

In this paper, six different additively manufactured heat exchangers with three different fin types are experimentally investigated. The heat exchangers are available in two versions each, which differ by a small

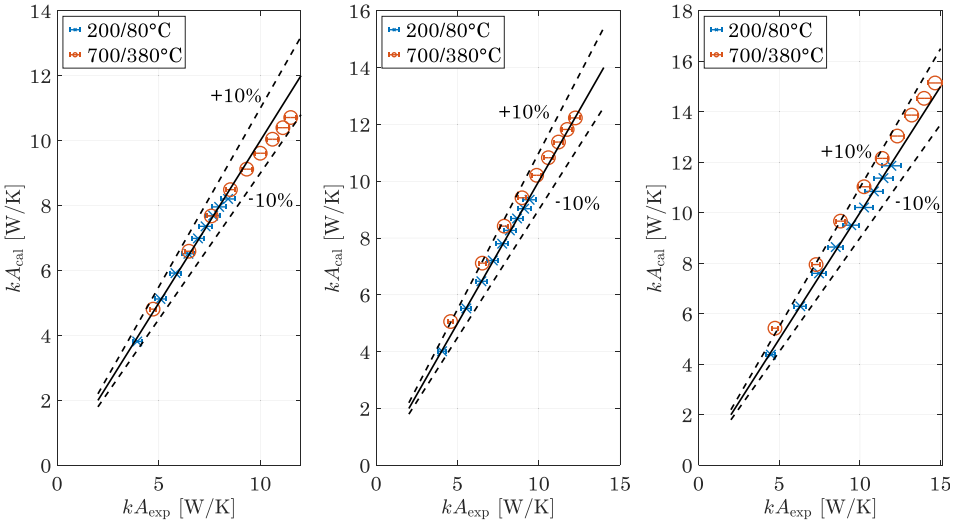

Fig. 18. Parity Plot of the overall heat transfer coefficient for 200/80 °C and 700/380 °C for the different fin types: left: „Ref"", middle: "FO", right: "HTO". Optimization at 200/80 °C.

modification at the fin tips, which increases the manufacturing quality significantly. The investigations are carried out at three temperature levels (200/80°C, 400/80°C and 700/380°C) and Reynolds numbers between 60 and 600. The analysis of the manufacturing quality of the fins shows significant differences between the laser-facing (top side) and laser-apart sides (bottom side). The top-side shows significantly better overall agreement with the CAD model, with a maximum deviation of +20% and a mean deviation of ∼+8%. The bottom side shows a significantly larger scatter of up to +42% of the fin thickness and +24% on average. The surface roughness analysis differs significantly between the top and bottom surfaces. On the top side, roughness's of $R_z = 25.2\ \mu$m on average are measured, while the bottom side shows roughness's of $R_z = 63.1\ \mu$m. For the evaluation of the heat transfer measurement results, a program is developed which takes into account the influence of axial heat conduction in the solid. The program is then used to determine the Nusselt numbers of the hot and cold sides and other parameters for the different heat exchangers and versions on the basis of the measured overall heat transfer coefficients by applying a combination of genetic algorithm and a gradient-based method. The analysis shows for the heat exchangers of version 1 on average $20 - 30$ % higher Nusselt numbers and $80 - 110$ % higher Fanning f-factors compared to the modified version 2. The analysis shows that the manufacturing inaccuracies result in a systematic, almost Reynolds number independent deviation of the Nusselt numbers and f-factors, which are attributed to a constant reduced hydraulic diameter. The detailed analysis of the heat exchangers in version 2 shows good to very good agreement with the numerically determined values for all heat exchangers. With increasing Reynolds numbers, an increasing deviation from the numerically determined values of maximum $10 - 15$ % is measured for the f-factors, which is attributed to increasing turbulence and an associated increasing influence of the surface roughness. The Nusselt numbers show very good agreement with the numerically determined data for all three heat exchangers over the entire Reynolds number range. The increasing influence of the surface roughness cannot be determined here. Also the modifications on the heat transferring fins can be captured correctly by the printer. The influences of thermal radiation on the overall performance of the heat exchangers are in the mid-single-digit percentage range; only for very low mass flows are influences of almost -10% on the heat transfer coefficient recorded. This is due in particular to heat radiation in the axial direction, which leads to a slight flattening of the temperature profile and thus to lower thermal performance.

All in all, the investigations in this article show that already small adjustments during the design process can have a huge impact on the heat transfer and pressure drop of additive manufactured heat exchangers. When these aspects are taking into account the predictability of the Nusselt number and the f-factor with numerical simulations in the laminar flow regime is very high. The investigations also show that the influence of the surface roughness is of minor importance, while the influence of the hydraulic diameter is to be rated significantly higher.

Declaration of Competing Interest

The authors declare no conflict of interest.

Data availability

Data will be made available on request.

Acknowledgment

The authors would like to express their gratitude to the Federal Ministry for Economic Affairs and Climate Action (BMWK) based on a resolution of the German Bundestag and AiF Projekt GmbH, grant number "KK5174901SN0" for supporting this research.

References

[1] B. Shen, Y. Li, H. Yan, S.K.S. Boetcher, G. Xie, Heat transfer enhancement of wedge-shaped channels by replacing pin fins with Kagome lattice structures, International Journal of Heat and Mass Transfer 141 (2019) 88–101, https://doi.org/10.1016/j.ijheatmasstransfer.2019.06.059.

[2] P. Ekade, S. Krishnan, Fluid flow and heat transfer characteristics of octet truss lattice geometry, International Journal of Thermal Sciences 137 (2019) 253–261, https://doi.org/10.1016/j.ijthermalsci.2018.11.031.

[3] D. Liang, G. He, W. Chen, Y. Chen, M.K. Chyu, Fluid flow and heat transfer performance for micro-lattice structures fabricated by Selective Laser Melting, International Journal of Thermal Sciences 172 (2022), 107312, https://doi.org/10.1016/j.ijthermalsci.2021.107312.

[4] T. Dixit, E. Al-Hajri, M.C. Paul, P. Nithiarasu, S. Kumar, High performance, microarchitected, compact heat exchanger enabled by 3D printing, Applied Thermal Engineering 210 (2022), 118339, https://doi.org/10.1016/j.applthermaleng.2022.118339.

[5] W. Tang, et al., Analysis on the convective heat transfer process and performance evaluation of Triply Periodic Minimal Surface (TPMS) based on Diamond, Gyroid and Iwp, International Journal of Heat and Mass Transfer 201 (2023), 123642, https://doi.org/10.1016/j.ijheatmasstransfer.2022.123642.

[6] L. Dassi, S. Chatterton, P. Parenti, A. Vania, B.M. Colosimo, P. Pennacchi, Cooled pads with bioinspired gyroid lattice for tilting pad journal bearings: Experimental validation of numerical model for heat transfer, Tribology International 184 (2023), 108448, https://doi.org/10.1016/j.triboint.2023.108448.
[7] J. Alexandersen, O. Sigmund, K.E. Meyer, B.S. Lazarov, Design of passive coolers for light-emitting diode lamps using topology optimisation, International Journal of Heat and Mass Transfer 122 (2018) 138–149, https://doi.org/10.1016/j.ijheatmasstransfer.2018.01.103.
[8] E.M. Dede, S.N. Joshi, F. Zhou, Topology Optimization, Additive Layer Manufacturing, and Experimental Testing of an Air-Cooled Heat Sink, Journal of Mechanical Design 137 (11) (2015), 111403, https://doi.org/10.1115/1.4030989.
[9] A.N. Pilagatti, G. Piscopo, E. Atzeni, L. Iuliano, A. Salmi, Design of additive manufactured passive heat sinks for electronics, Journal of Manufacturing Processes 64 (2021) 878–888, https://doi.org/10.1016/j.jmapro.2021.01.035.
[10] T. Dbouk, A review about the engineering design of optimal heat transfer systems using topology optimization, Applied Thermal Engineering 112 (2017) 841–854, https://doi.org/10.1016/j.applthermaleng.2016.10.134.
[11] M. Bichnevicius, D. Saltzman, S. Lynch, Comparison of Additively Manufactured Louvered Plate-Fin Heat Exchangers, Journal of Thermal Science and Engineering Applications 12 (1) (2020), 011018, https://doi.org/10.1115/1.4044348.
[12] A. Vafadar, F. Guzzomi, K. Hayward, Experimental Investigation and Comparison of the Thermal Performance of Additively and Conventionally Manufactured Heat Exchangers, Metals 11 (4) (2021) 574, https://doi.org/10.3390/met11040574.
[13] S.A. Niknam, M. Mortazavi, D. Li, Additively manufactured heat exchangers: a review on opportunities and challenges, Int J Adv Manuf Technol 112 (3-4) (2021) 601–618, https://doi.org/10.1007/s00170-020-06372-w.
[14] D. Saltzman, S. Lynch, Flow-Field Measurements in a Metal Additively Manufactured Offset Strip Fin Array Using Laser Doppler Velocimetry, Journal of Fluids Engineering 143 (4) (2021), 041502, https://doi.org/10.1115/1.4049245.
[15] D. Saltzman, S. Lynch, Overall Pressure Loss and Heat Transfer Performance of Additively Manufactured Offset Strip Fins Used in Compact Heat Exchangers, Journal of Thermal Science and Engineering Applications 14 (12) (2022), 120902, https://doi.org/10.1115/1.4053929.
[16] K. Huang, J.W. Wan, C.X. Chen, Y.Q. Li, D.F. Mao, M.Y. Zhang, Experimental investigation on friction factor in pipes with large roughness, Experimental Thermal and Fluid Science 50 (2013) 147–153, https://doi.org/10.1016/j.expthermflusci.2013.06.002.
[17] J. Ning, et al., Experimental and numerical investigation of additively manufactured novel compact plate-fin heat exchanger, International Journal of Heat and Mass Transfer 190 (2022), 122818, https://doi.org/10.1016/j.ijheatmasstransfer.2022.122818.
[18] L. Prandtl, K. Oswatitsch, K. Wieghardt, Führer Durch Die Strömungslehre, Vieweg +Teubner Verlag, Wiesbaden, 1990, https://doi.org/10.1007/978-3-322-99491-2.
[19] M. Fuchs, N. Lubos, S. Kabelac, Numerical Calculation of the Irreversible Entropy Production of Additively Manufacturable Off-Set Strip Fin Heat-Transferring Structures, Entropy 25 (1) (2023) 162, https://doi.org/10.3390/e25010162.
[20] Zeiss GOM Inspector, 2022. https://www.gom.com/de-de/produkte/zeiss-quality-suite/gom-inspect-pro.
[21] D. Saltzman, et al., Design and evaluation of an additively manufactured aircraft heat exchanger, Applied Thermal Engineering 138 (Jun. 2018) 254–263, https://doi.org/10.1016/j.applthermaleng.2018.04.032.
[22] F. Battaglia, X. Zhang, M.A. Arie, A. Shooshtari, A. Sarmiento, M. Ohadi, Additive Manufacturing of a High Temperature, Ni-Based Superalloy Compact Heat Exchanger: A Study On the Role of Select Key Printing Parameters, Journal of Heat Transfer (2022) 1–36, https://doi.org/10.1115/1.4056484.
[23] P. Stephan, S. Kabelac, M. Kind, D. Mewes, K. Schaber, T. Wetzel (Eds.), VDI-Wärmeatlas: Fachlicher Träger VDI-Gesellschaft Verfahrenstechnik und Chemieingenieurwesen, Springer Reference Technik. Berlin, Heidelberg: Springer Berlin Heidelberg, 2019, https://doi.org/10.1007/978-3-662-52989-8.
[24] W.M. Kays, Loss Coefficients for Abrupt Changes in Flow Cross Section With Low Reynolds Number Flow in Single and Multiple-Tube Systems, Journal of Fluids Engineering 72 (8) (1950) 1067–1074, https://doi.org/10.1115/1.4016919.
[25] M. Fuchs, X. Luo, S. Kabelac, Influence of axial heat conduction in solid walls and fins on the overall thermal performance of an additively manufactured high-temperature heat exchanger, Applied Thermal Engineering 212 (2022), 118566, https://doi.org/10.1016/j.applthermaleng.2022.118566.
[26] R.M. Manglik, A.E. Bergles, Heat transfer and pressure drop correlations for the rectangular offset strip fin compact heat exchanger, Experimental Thermal and Fluid Science 10 (2) (1995), https://doi.org/10.1016/0894-1777(94)00096-Q. Art. no. 2, Feb.
[27] H.M. Joshi, R.L. Webb, Heat transfer and friction in the offset stripfin heat exchanger, International Journal of Heat and Mass Transfer 30 (1) (1987), https://doi.org/10.1016/0017-9310(87)90061-5. Art. no. 1, Jan.
[28] R. Chennu, Steady state and transient analysis of compact plate-fin heat exchanger fins for generation of design data using CFD, Int Jnl of Num Meth for HFF 26 (2) (2016), https://doi.org/10.1108/HFF-01-2015-0039. Art. no. 2, Mar.
[29] H.D. Baehr, K. Stephan, Wärme- und Stoffübertragung, Springer Berlin Heidelberg, Berlin, Heidelberg, 2013, https://doi.org/10.1007/978-3-642-36558-4.
[30] M. Fuchs, S. Kabelac, Numerical Calculation of the Irreversible Entropy Production in Heat Transferring Structures, Chemie Ingenieur Technik 95 (5) (2023) 692–700, https://doi.org/10.1002/cite.202200213.
[31] J.W. Rose, Heat-transfer coefficients, Wilson plots and accuracy of thermal measurements, Experimental Thermal and Fluid Science 28 (2–3) (2004) 77–86, https://doi.org/10.1016/S0894-1777(03)00025-6.
[32] H.F. Khartabil, R.N. Christensen, An improved scheme for determining heat transfer correlations from heat exchanger regression models with three unknowns, Experimental Thermal and Fluid Science 5 (6) (1992) 808–819, https://doi.org/10.1016/0894-1777(92)90125-O.
[33] R. Steinhoff, X. Luo, S. Kabelac, Condensation heat transfer of R-134A on single horizontal three-dimensional structured tubes, in: International Heat Transfer Conference 16, Begellhouse, Beijing, China, 2018, pp. 2485–2492, https://doi.org/10.1615/IHTC16.cod.023874.
[34] Mathworks, 'Genetic Algorithm Matlab R2021b', May 16, 2023. https://de.mathworks.com/help/gads/how-the-genetic-algorithm-works.html.
[35] Mathworks, 'Options for Genetic Algorithm Matlab R2021b', May 16, 2023. https://de.mathworks.com/help/gads/genetic-algorithm-options.html.
[36] Evaluation of measurement data - Guide to the expression of uncertainty in measurement, Joint Committee for Guides in Metrology (2008).
[37] J. Sieres, A. Campo, Uncertainty analysis for the experimental estimation of heat transfer correlations combining the Wilson plot method and the Monte Carlo technique, International Journal of Thermal Sciences 129 (2018) 309–319, https://doi.org/10.1016/j.ijthermalsci.2018.03.019.
[38] R. Chennu, Numerical analysis of compact plate-fin heat exchangers for aerospace applications, HFF 28 (2) (2018), https://doi.org/10.1108/HFF-08-2016-0313. Art. no. 2, Feb.
[39] X. Luo, G.Y. Zhou, L.W. Cong, M. Fuchs, S. Kabelac, Numerical Simulation of Heat Transfer and Fluid Flow in 3D-Printed High-Temperature Plate-Fin Heat Exchangers with OpenFoam, in: Proceeding of Proceedings of the 25th National and 3rd International ISHMT-ASTFE Heat and Mass Transfer Conference (IHMTC-2019), Begellhouse, IIT Roorkee, Roorkee, India, 2019, pp. 569–574, https://doi.org/10.1615/IHMTC-2019.960.
[40] R. Span, E.W. Lemmon, R.T. Jacobsen, W. Wagner, A. Yokozeki, A Reference Equation of State for the Thermodynamic Properties of Nitrogen for Temperatures from 63.151 to 1000 K and Pressures to 2200 MPa, Journal of Physical and Chemical Reference Data 29 (6) (2000) 1361–1433, https://doi.org/10.1063/1.1349047.
[41] T.H. Chung, M. Ajlan, L.L. Lee, K.E. Starling, Generalized multiparameter correlation for nonpolar and polar fluid transport properties, Ind. Eng. Chem. Res. 27 (4) (1988) 671–679, https://doi.org/10.1021/ie00076a024.